FIBER OPTIC MICRO-ENDOSCOPY FOR DETECTION OF BACTERIA IN EARLY STAGES OF INFECTION

A Thesis

by

NOOMAN SADAT MUFTI

Submitted to the Office of Graduate Studies of
Texas A&M University
in partial fulfillment of the requirements for the degree of

MASTER OF SCIENCE

December 2010

Major Subject: Biomedical Engineering

Fiber Optic Micro-endoscopy for Detection of Bacteria in Early Stages of Infection

Copyright 2010 Nooman Sadat Mufti

FIBER OPTIC MICRO-ENDOSCOPY FOR DETECTION OF BACTERIA IN EARLY STAGES OF INFECTION

A Thesis

by

NOOMAN SADAT MUFTI

Submitted to the Office of Graduate Studies of
Texas A&M University
in partial fulfillment of the requirements for the degree of

MASTER OF SCIENCE

Approved by:

Chair of Committee,	Kristen Carlson Maitland
Committee Members,	Jeffrey Cirillo
	Kenith Meissner
Head of Department,	Gerard Coté

December 2010

Major Subject: Biomedical Engineering

ABSTRACT

Fiber Optic Micro-endoscopy for Detection of Bacteria in Early Stages of Infection.

(December 2010)

Nooman Sadat Mufti, B.Tech, Aligarh Muslim University, India;

M.S., National University of Singapore-MIT Alliance, Singapore

Chair of Advisory Committee: Dr. Kristen Carlson Maitland

Mycobacterium tuberculosis, the bacterium that causes tuberculosis, has an incubation period ranging from a few months to several years following infection via inhalation into the lungs. Whole body fluorescence scanners are used to image and monitor the growth of fluorescent protein expressing strains of *M. tuberculosis* in the lungs of animal models. Accurate quantitative analysis of bacterial growth during the early stages of infection inside lungs remains elusive, due to tissue absorption and scattering of photons emitted by the low numbers of bacteria deep in tissue.

Fiber optic micro-endoscopy is uniquely suited to provide a novel solution to this problem by delivering light excitation directly to and collecting fluorescence from the infection site located in the lungs of an animal model, thereby enabling detection of fluorescent bacteria during the early stages of infection. In this thesis, I present a contact probe fiber bundle fluorescence micro-endoscope with a range of LED based excitation wavelengths, 4 μm resolution, a 750 μm field of view, and a 1 mm outer diameter. This system has detected tdTomato and GFP expressing Bacillus Calmette-Guérin (BCG)

bacteria *in vitro.* Additionally, images of bacterial regions of infection obtained in mice subcutaneously infected with tdTomato expressing bacteria at concentrations ranging from 10^6 to 10^1 Colony Forming Units (CFU) and intra-tracheally infected mice at 10^6 CFU demonstrate the micro-endoscope's capability to detect and resolve regions of bacterial infection *in vivo*. By relaying the bacterial fluorescence image from the infection site to an external detector, we are able to increase the sensitivity to early stages of infection.

DEDICATION

To my parents, brother and friends

ACKNOWLEDGEMENTS

I would like to thank my committee chair, Dr. Kristen Maitland, and my committee members, Dr. Jeffrey Cirillo and Dr. Kenith Meissner, for their guidance and support throughout the course of this research. I want to extend my thanks to Dr. Ying Kong, my collaborator in the animal imaging study.

Thanks also go to my friends and colleagues and the department faculty and staff for making my time at Texas A&M University a great experience. I also extend my thanks to Rachel Schafer, an undergraduate student who worked with me initially on this project.

Finally, thanks to my mother, father, brother and the wonderful friends I made in College Station for their constant encouragement and support.

TABLE OF CONTENTS

Page

LIST OF FIGURES

Page

LIST OF TABLES

1. INTRODUCTION

Bacterial infections such as tuberculosis (TB) affect a large segment of the world's population; the Centers for Disease Control (CDC) estimates approximately one-third of the world's population is currently infected with TB. The disease has an incubation period that varies from a few weeks to years. TB is difficult to diagnose at an early stage and when it is detected following the onset of symptoms, it requires a cocktail of antibiotics in a strict regimen to completely cure a patient. Research into the study of the early detection and growth of bacterial infections such as tuberculosis is hence imperative [1].

A variety of clinical techniques exist for the detection of bacterial infections such as tuberculosis. These include the Monteux skin test, saliva tests, and X-ray diagnosis [2]. These detection techniques are plagued with either low specificity or the ability to only detect late stage infections. Moreover, more advanced molecular biology techniques such as polymerase chain reaction (PCR) and the enzyme linked immuno-sorbent assay (ELISA) [3-6] can provide highly accurate bacterial detection and quantification capabilities, but not in real time or *in vivo.*

Optical imaging and detection utilizes light to interrogate a sample and detects either the reflectance or fluorescence from various endogenous or exogenous molecules present, thereby providing a means of real-time and *in vivo* detection and imaging of biological samples. Researchers have developed optical biosensors that can detect in

---

This thesis follows the style of the Journal of Biomedical Optics.

various *ex vivo* samples [7-9]. Moreover, whole animal fluorescence imaging systems, have been developed which are able to image and quantify fluorescent bacterial infections from entire animals. These systems are being used for non-invasive *in vivo* pathogenesis studies of bacterial infections [10-14]. However, due to the depth of the infectious tissue, such as lung tissue in the case of tuberculosis, tissue absorption and scattering of photons emitted by the low numbers of bacteria present precludes the possibility of using these systems for early stage quantification of bacterial infections.

Micro-endoscopes that utilize fiber-optic elements to relay real-time reflectance or florescence signals from tissue and organs *in vivo* are in common use in the healthcare sector. They are also currently being developed and evaluated as tools to assist in guiding biopsies for the diagnosis of pre-cancer [15-16] and for *in vivo* pre-clinical brain imaging applications [17]. Such a fiber based fluorescence imaging system is uniquely suited for the detection and imaging of small regions of bacterial infection inside live animals. It can serve as a valuable tool to study the early stage *in vivo* dynamics of bacterial infection, especially when used in concert with whole body imaging systems.

This thesis highlights the significance of bacterial infections, such as TB and TB's currently understood mechanism of infection and pathogenesis. It delves into current technologies that are being researched for bacterial detection and imaging, with their merits and limitations. The fluorescence fiber-optic micro-endoscope that we have developed, based on a similar system [16], is described. The system characterization along with its ability to resolve cellular and tissue level features is established via images taken using common fluorescence dyes and dye-stained biological samples. Its utility in

imaging bacterial infections *in vitro* and *ex vivo* is then described in depth. Finally, recommendations for a system design to further improve the scope for the study of the physiological spread of tuberculosis and other bacterial agents in live animal models are presented.

2. BACKGROUND AND SIGNFICANCE

2.1 Tuberculosis

Tuberculosis (TB) is the leading cause of death in the world due to bacterial infection. It usually affects the lungs but can spread to various parts of the body. Roughly 1.8 billion people, close to one-third of the world's population, are infected with tuberculosis, and 9 million new cases are reported each year. Close to 2 million people worldwide die annually from tuberculosis. HIV is the leading predisposing factor for tuberculosis infection and 10 % of all HIV infected people harbor the disease. Tuberculosis is also the leading cause of death for HIV infected people [1].

The active disease is characterized by a chronic cough that is accompanied with blood filled sputum, fever and weight loss. The disease spreads when someone with active TB coughs, sneezes or sings, thereby releasing the aerosolized form of the bacteria into the air that can be inhaled by people nearby. The bacterium has an incubation period that can range from a few months to a few years following the time of infection via inhalation into the lungs, making it difficult for the disease to be detected early on in the infection [1-2].

Mycobacterium tuberculosis (MTB), the bacterium responsible for tuberculosis is rod shaped, 2-4 μm in length, and 0.2-0.5 μm in width as can be seen from the scanning electron micrograph (SEM) image (Figure 1, [2]). The disease is spread by droplet nuclei 1-5 μm in diameter released during expectoration from a patient with pulmonary or laryngeal tuberculosis. Most of these bacilli get lodged in the nose and throat while some

of them are taken up and get lodged in the alveoli of the bronchi. Alveolar macrophages non-specifically uptake these bacilli, but since they are not activated, they are not able to kill the bacteria.

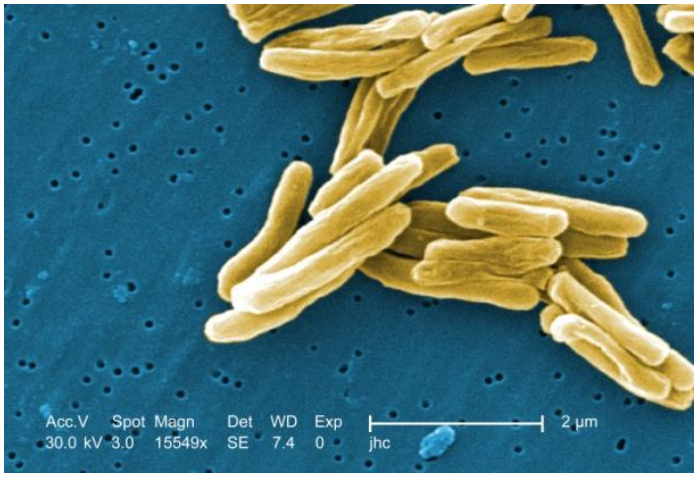

Figure 1: Scanning electron micrograph image of *Mycobacterium tuberculosis* (Centers for Disease Control) [2].

One to three weeks post-infection, MTB multiplies without restriction inside the inactive macrophages, which then burst, spewing out their bacterial load. Other macrophages then get attracted and extravasate to phagocytose these bacilli, but due to their inactivation, are not able to eliminate the MTB.

During stage 3 of the infection, T-cell lymphocyte activation of macrophages enables them to kill the bacteria and control the infection via cell mediated immunity. This tuberculin-positive stage can be detected via the Monteux skin test. Tubercle (lump) formation then takes place when the bacteria are enclosed in a hardened mass. The center of the tubercle attains a caseate or cheesy consistency which prevents MTB growth due to its low pH and anoxic environment. The MTB can however persist in these tubercles for very long periods.

During stage 4 of the infection, various inactivated macrophages surrounding the tubercles are co-opted by MTB to replicate. This enables the tubercle to grow and invade neighboring bronchi and spread to other parts of the lung, a pulmonary spread of the disease. The growing tubercle may even reach arteries or blood vessels and enable hematogenous spread of the bacteria, an extra-pulmonary spread of the disease. This can result in the formation of secondary lesions mostly in the genitourinary system, bones, joints, lymph nodes and peritoneum. The lesions can be either exudative, in which the bacteria can multiply without restriction in a 'soft' tubercle, or they can be granulomatous, in which the host's hypersensitivity results in the formation of a hard tubercle that can effectively restrict bacterial growth.

In stage 5 of the infection, the caseous centers of the tubercles liquefy to produce a very conducive medium enabling rapid MTB extracellular growth. This causes the nearby bronchi to become necrotic and results in cavity formation, allowing the MTB to spread by spilling into it. Only a small percentage of MTB infections cause disease. Typically when the primary lesions heal by fibrosis and calcification, they form a Ghon's complex, a calcified focus of infection and an associated lymph node, which is readily visible in a chest X-ray. They may rarely contain viable bacteria and can be a source of the re-activation of the disease later in life. Some metastatic calcified foci containing low numbers of viable MTB, known as Simon foci are typically the source of disease re-activation [2, 18-20].

Green fluorescent protein (GFP) complimentary-DNA (cDNA) carrying shuttle plasmid vector have been constructed with transcription fusion with promoters of

interest and introduced via electroporation into *M. tuberculosis* and *bovis* Bacillus Calmette-Guérin (BCG) to create transformed fluorescent bacteria [21]. Exposure to antibiotics kills off any bacteria that have not been transformed. Such transfected GFP expressing bacteria have been used to study pathogenesis of living tissue [10] and are even being used as novel fluorescent biosensors based on bacterial response to global class of environmental effectors, nutrients or toxins [22].

2.2 Detection of bacteria

Various devices have been made for the rapid detection of bacteria in biological samples such as blood, saliva, food, and the environment. Taniguchi *et al.* [7] have developed a fiber optic immuno-sensor with a Cyanine-5 (Cy5) labeled polyclonal antibody as the detection element immobilized on a polystyrene optical fiber (Figures 2 A and B).

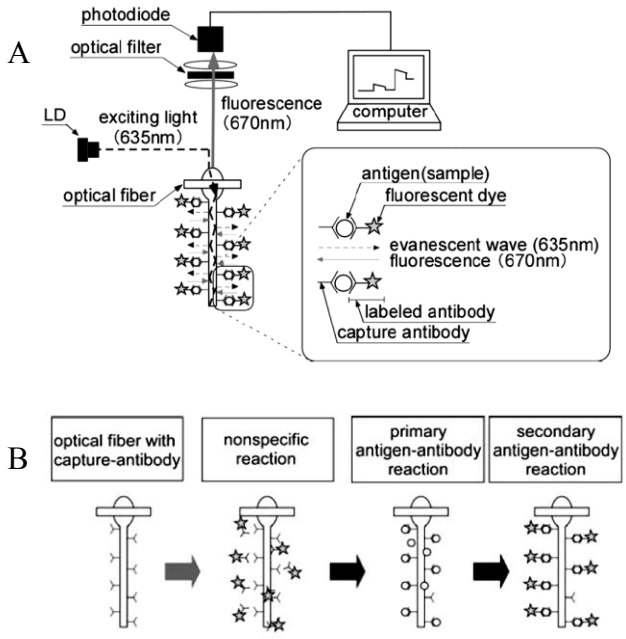

Figure 2: A) Fluorescent immune-assay using an optical fiber [7]; B) process of bacterial immuno-sensing [7].

Evanescent light from the illuminated fiber excites the Cy5 molecules and the fluorescence is collected via a photodiode. The device has been used to detect *Escherichia coli* and *Listeria* monocytogenes in samples. Rapid bacterial identification has been performed via the study of the auto-fluorescence spectra of different bacterial species like *Escherichia coli*, *Enterococcus faecalis,* and *Staphylococcus aureus* by employing excitation light ranging from 330 to 510 nm and employing principal component analysis to the detected fluorescence spectra [9]. Other groups are studying the activity of bacteria like *Streptococcus mutans* (the agent responsible for dental caries) in bodily fluids like saliva using the exponential decay of the evanescent wave at the fiber core-dye encapsulating gel interface [8]. These techniques are very useful as portable biosensors for on-site monitoring and detection of bacteria but cannot be used for the *in vivo* detection and imaging of bacterial progression in real time.

2.3 Pathogenesis studies

Whole body fluorescence scanners, such as the Caliper Life Sciences In-Vivo Imaging System (IVIS Spectrum), have been employed for *in vivo* preclinical imaging applications, including the study of disease progression and gene expression by employing co-expression of fluorescent markers. These systems are extensively used for the non-invasive detection and growth monitoring of tumors and the effects of chemotherapy on tumor size [23-24]. Similarly, for the detection and imaging of bacteria, genetically transfected strains of various bacteria such as GFP expressing *Mycobacterium smegmatis* and *bovis* have been developed [21]. Colonization dynamics of *C. rodentium* and *E. coli* [12] have been studied using whole body imaging at

detection limits down to 10^3 CFU for gut localized bacteria. Entire bacterial biofilms have also been detected through macroscopic imaging using the IVIS [11].

Real-time, *in vivo* monitoring of bacterial infection occurring at chronic subcutaneous and intra-muscular prosthetic implant sites using bioluminescent *Staphylococcal aureus* bacteria prior to and following treatment with antibiotics is also being investigated (Figure 3) [14].

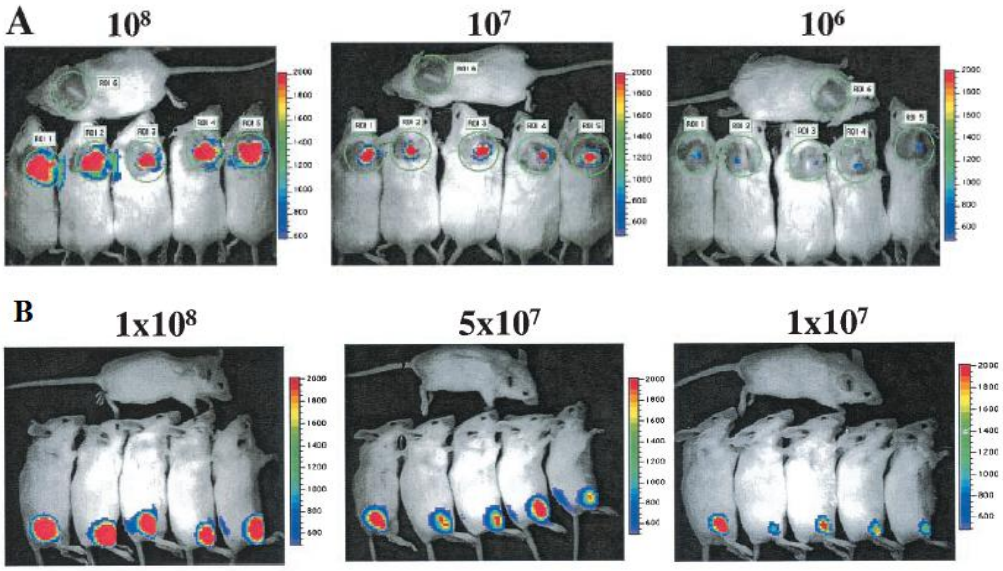

Figure 3: Macroscopic images of bioluminescent *S. aureus*, A) subcutaneously infected; B) intra-muscularly infected [14].

Macroscopic imaging detection limits determined through the studies were 10^5 CFU for subcutaneous infection (Figure 3 A) and 10^6 CFU (Figure 3 B) for intra-muscular infection. Long term pneumococcal infections in the lungs of living mice have been conducted using bioluminescent *Streptococcus pneumoniae* transformed with a gram-positive lux transposon [13]. Kong *et al.* have employed optical imaging using the IVIS Spectrum to study the extrapulmonary spread of tuberculosis after an initial

intranasal infection in mice [10]. They have determined that the *in vitro* detection limit for tdTomato expressing bacteria has a ten-fold improvement as compared to enhanced GFP (EGFP). On using the higher quantum yield tdTomato expressing bacteria, they also determined via subcutaneous infection imaging tests that this system can image and quantify mycobacteria at dosage levels greater than 10^5 CFU. Owing to the highly scattering nature of the lungs, to study pulmonary infections, intranasal dosage levels greater than 10^5 CFU are typically employed to study pulmonary infections. However, intranasal dosage levels greater than 10^4 CFU result in extra-pulmonary spread from the lungs with non-physiological growth kinetics. Detection limits for various types of bacterial infection are summarized in Table 1. Until now, accurate quantitative analysis of bacterial growth during the early stages of infection in the lungs and at low bacterial concentrations has not been possible, primarily due to scattering and tissue absorption of photons emitted from the low numbers of fluorescent bacteria present deep in the tissue. A need arises for a system that can image and quantify pulmonary bacterial infection at inoculums below 10^5 CFU during the first few days following infection to model early stage and low bacterial load infection. The system must also be able to image below 10^4 CFU for the study of the physiological spread of the infection into extra-pulmonary areas. To my knowledge, no fiber based micro-endoscopes have been used previously for studying bacterial infection.

Table 1: Bacterial detection limits using whole animal imaging scanners.

Reference	Bacteria	Inoculation dose	Luminescence modality	Detection limit	Location of bacteria/infection
[12]	*Citrobacter rodentium*	10^9 CFU (oral)	Bioluminescent	10^3 CFU	*In vivo (gut)*
[14]	*S. aureus*	10^6-10^8 CFU (subcutaneous catheter implant, thigh injection)	Bioluminescent	10^5 CFU (subcutaneous), 10^6 CFU (muscle)	*In vivo* (subcutaneous, muscle tissue)
[10]	*M.bovis BCG*	10^1- 10^7 CFU	Fluorescence (EGFP)	10^3 CFU	*In vitro*
[10]	*M. bovis BCG*	10^1- 10^7 CFU	Fluorescence (tdTomato)	10^2 CFU	*In vitro*
[10]	*M. bovis BCG*	10^4-10^7CFU (subcutaneous)	Fluorescence (EGFP)	10^7 CFU	*In vivo* (subcutaneous)
[10]	*M. bovis BCG*	10^4-10^7CFU (subcutaneous)	Fluorescence (tdTomato)	10^5 CFU	*In vivo* (subcutaneous)

2.4 Fiber bundle micro-endoscopes

2.4.1 Optical fluorescence microscopy

Fluorescence microscopy is a widely used technique in biology. Excitation light in an epi-illumination or Ploem illumination configuration is first reflected off a dichroic mirror and focused by an objective lens onto a fluorescent sample. The fluorescence from the sample, which occurs at wavelengths longer than the excitation, is then collected by the same objective and focused onto a detector using a lens (Figure 4, [25]). Since most of the excitation light passes through the sample, only reflected excitation light and emitted light is collected by the objective. In combination with an emission filter placed before the detector, this serves to provide a very high signal-to-noise ratio.

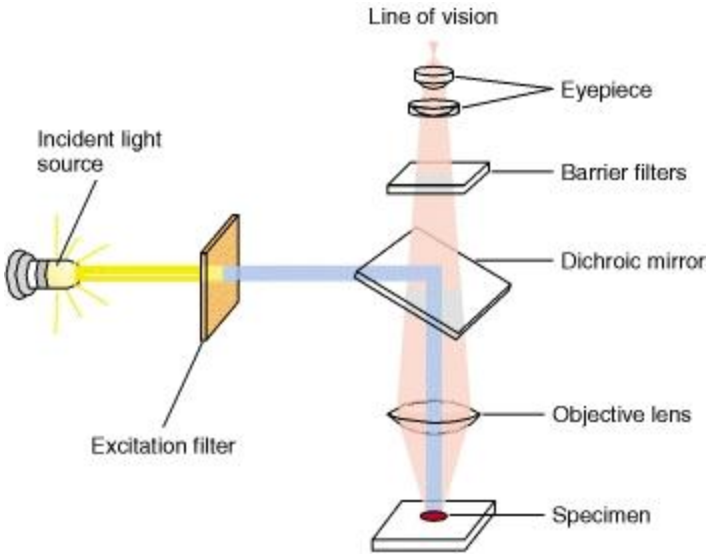

Figure 4: Epi-fluorescence microscope setup (Molecular Cell Biology, [25]).

The theoretical maximum resolution of a fluorescence microscope is the Abbe or diffraction limited focused spot size, equal to one-half of the wavelength of the light used (0.26 μm for a 520 nm GFP emission). This is also the shortest distance between the maxima of the point spread functions or Airy disks formed from 2 individual points of light from the sample that can be distinguished by the optical system. The resolution of the optical system is defined by $r = 0.61\ x\ \lambda/\mathrm{NA}$, where λ is the wavelength of light and NA is the numerical aperture of the objective and condenser lenses used [26].

2.4.2 Micro-endoscopy

Micro-endoscopes employing a scanning mechanism at the distal end of a single-mode fiber have been developed having a lateral resolution of 0.8 μm and confocal sectioning ability due to the fiber acting as a confocal pin-hole [27]. Fiber bundle micro-endoscopes involve the use of a coherent fiber bundle, comprising thousands of individual fibers, with the proximal end placed after the objective lens to collect the

focused excitation light. The distal end of the fiber, which is placed in contact with the fluorescent sample, relays the fluorescent signal back onto the same objective lens. The advantage of using a fiber bundle in place of a single-mode fiber is that the need for a distal end scanning mechanism is eliminated and the use of wide field illumination and fluorescence collection via the same bundle obviates the need for a scanning mechanism altogether. The core to core spacing of the fiber elements determines the limit of the lateral resolution of the system and the active imaging bundle area determines the field-of-view of the system. For instance, for a typical Sumitomo IGN-08/30, a 0.9 mm outer diameter fiber bundle comprising approximately 30000 fibers, with a core size of 2.2 μm and a core-to-core spacing of 4 μm [28], the lateral resolution determined is approximately 4 μm with a 750 μm field-of-view.

A fiber optic plate microscope comprising a contact probe fiber bundle coupled with a conventional fluorescence microscope was first reported for *in vivo* imaging of brain structure and physiological activity (Figure 5 A and B) [17, 29]. Fiber bundle optic micro-endoscopes have since been used for diverse applications including the *in vivo* imaging of tumors and for pre-cancer detection in epithelial cells and tissue in the oral mucosa [16].

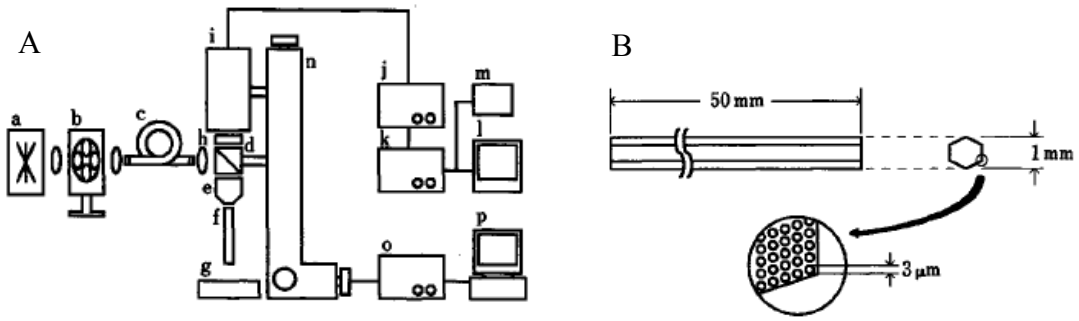

Figure 5: A) Schematic of the fiber-optic plate microscope system. a, xenon lamp; b and h, filters; c, bundle optical fiber; d, dichroic mirror e, objective lens; f, fiber-optic plate; i, ICCD camera; l, color monitor; B) Fiber optic plate schematic: The fiber-optic plate is 50 mm in length and 1 mm in diameter. It is comprised of thousands of optical fibers, 3 μm in diameter with a core-to-core spacing of 3 μm, which determines the lateral resolution of the system [17, 29].

Muldoon *et al*. have built a wide field Light Emitting Diode (LED) illumination based, 1 mm diameter fiber bundle micro-endoscope capable of sub-cellular resolution imaging (4 μm resolution with 750 μm field of view) for pre-cancer detection in the oral mucosa [16]. Fiber optic confocal fluorescence micro-endoscopes have also been developed that employ a scanning mechanism at the proximal fiber bundle end and utilize each fiber element as a pin-hole to remove out-of-focus light, thereby enabling optical sectioning [15, 30]. They have been used for pre-cancer detection using morphology discrimination by imaging epithelial cells from cervical tissue, fluorescence lifetime imaging for biochemical analysis [31], as well as the morphological and functional imaging of *in vivo* microvasculature [32]. Confocal fluorescence micro-endoscopes have also been modified for spectroscopy and multispectral imaging of varied dye stained samples [33-34]. These systems have the advantage of high resolution by optical sectioning but at the expense of loss of signal with removal of scattered light. Wide-field contact-probe fluorescence micro-endoscopes have a much less complex, non-scanning system design and collect scattered fluorescence, which improves

sensitivity, but at the cost of resolution. Although major advances in optical fiber based high resolution *in vivo* imaging systems have been achieved in the field of early cancer detection, to my knowledge, fiber optic micro-endoscopy has not yet been applied to *in vivo* imaging and detection of bacteria.

Tuberculosis is a global health issue and knowledge of its early growth kinetics and pathogenesis which is essential to effectively combat it, is limited. Wide field optical imaging techniques are being used to study pathogenesis but do not provide an accurate analysis of bacterial growth at early stages of infection and at low bacterial concentrations. Moreover, low resolution, low sensitivity fiber based systems have been used for bacterial detection, but not for imaging. Fiber bundle micro-endoscopes have the potential to provide a unique imaging platform for studying early stages of bacterial infection and at low concentrations.

3. SYSTEM DESIGN

3.1 Micro-endoscope setup

A contact probe based fiber optic micro-endoscope, capable of providing efficient excitation and collection of fluorescence light from regions of bacterial infection, was designed, constructed and optimized. The resulting setup was capable of imaging and resolving bacterial colonies *in vitro* and regions of infection in excised subcutaneous and lung tissue.

3.1.1 Fluorescence mode

Figure 6 illustrates the layout of the fluorescence micro-endoscope, the basic design of which is modeled after the system described in the background section [16]. Excitation light from the LED source is collimated by a lens and filtered by an excitation filter, if necessary, to obtain a narrow wavelength band. The excitation light is then reflected by a dichroic mirror and focused by an objective lens onto a fiber bundle. The fiber bundle transmits the excitation light to its distal tip, which is placed in contact with the sample. The resulting fluorescence light from the sample is collected by the same fiber bundle, filtered by emission filters, and imaged onto a scientific grade CCD camera (QImaging Exi Blue, 1.45 Mpixels, 6.45 μm x 6.45 μm pixel size).

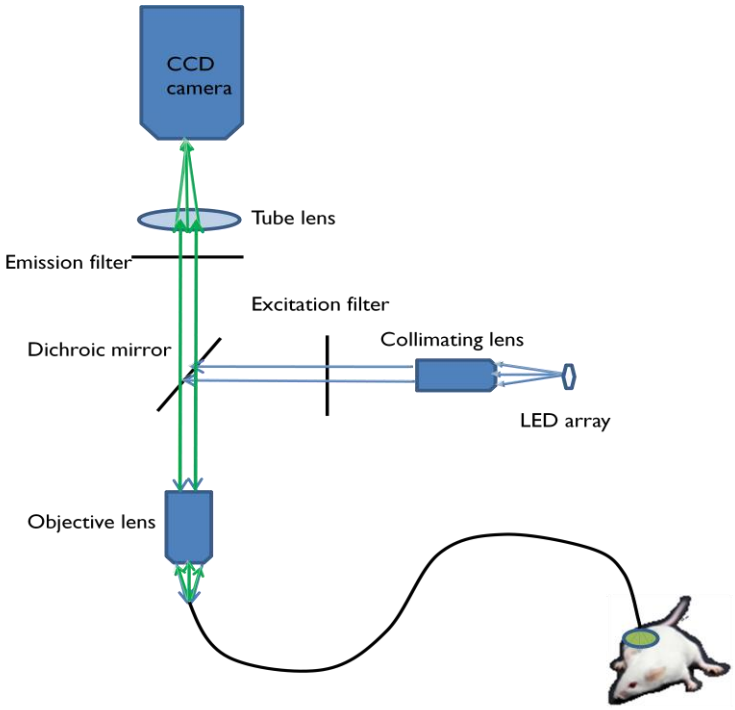

Figure 6: Schematic of fluorescence micro-endoscope for preclinical imaging.

The tube lens (150 mm focal length, Thorlabs achromatic doublet) in concert with an 18.2 mm focal length, 10x Leica objective lens, provides a magnification of 8.2*x* (determined by the ratio of the focal length of the tube lens to the focal length of the objective) to focus the entire 750 µm active area of the fiber bundle onto the 2/3 inch (diagonal) CCD camera. The system has a range of LED based excitation wavelengths to excite various fluorophores with corresponding dichroic, excitation and emission filters procured from Chroma technologies mounted on filter wheels (Table 2). The resolution of the system, determined by the fiber core-to-core spacing specification of 4 µm and the field-of-view, determined by the active imaging area of the 1mm outer diameter fiber bundle is 750 µm. Figure 7 illustrates the top and side views of the constructed system.

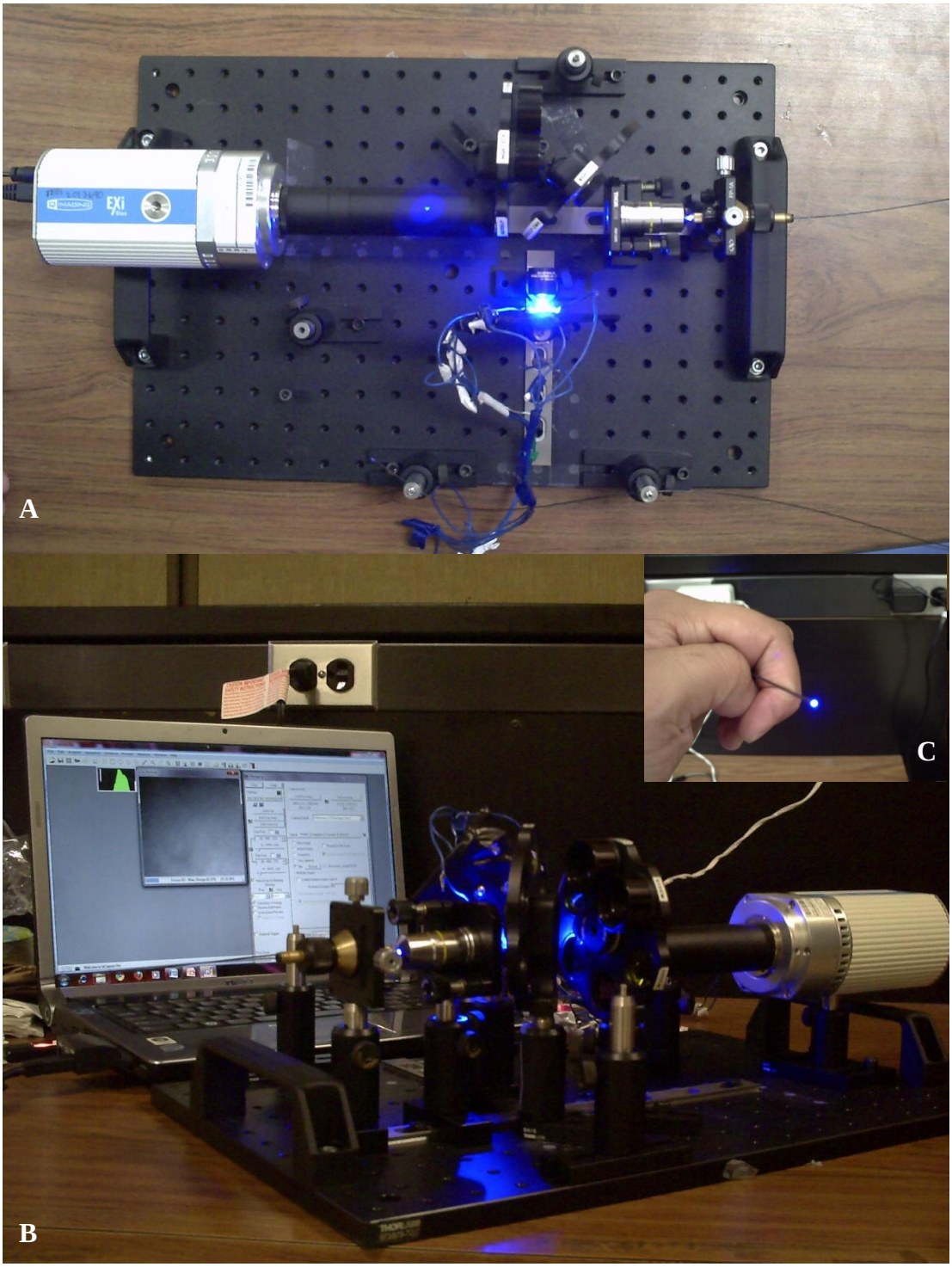

Figure 7: A) Top-view of the fluorescence micro-endoscope system; B) side-view of system; C) inset image of the distal (imaging) end of probe.

Table 2: LED and filter wavelengths for various fluorophores.

LED excitation wavelength (nm)	Dichroic mirror cut-on wavelength (nm)	Band pass excitation filter center wavelength (nm) (if applicable)	Emission filter cut on wavelength (nm)	Fluorescent proteins and dyes
470	495	470 40 nm BW	505	tdTomato, mKeima, EGFP, Acridine Orange, Fluorescein
590	600	NA	610	mCherry, mKate, mKeima
680	690	NA	700	Cy5.5
790	800	NA	810	IrDye

3.1.2 Reflectance mode

The system can also be configured in reflectance mode by replacing the dichroic mirror with a beam splitter and swapping the excitation and emission filters with crossed polarizers. The excitation light incident on the fiber bundle is polarized. Back reflection from the proximal bundle surface is removed by the crossed polarizer. Light that travels to the distal tip of the bundle experiences scattering and loss of polarization in the tissue, allowing signal to pass through the crossed polarizer and onto the CCD.

3.2 Selection of optical elements

Efficient coupling of excitation light from the LED into the fiber bundle is critical to increase illumination of the sample and subsequent fluorescence signal for detection. Furthermore, a higher excitation power at the distal tip enables greater penetration of the light into the tissue. This will be essential for imaging at a specific depth in the tissue through the addition of an objective lens on the fiber tip, which is planned as a future modification of the system.

3.2.1 Selection of LEDs

LEDs were chosen with the minimum possible divergence angle at the highest available output power so as to maximize the optical coupling into the fiber bundle. LEDs from Roithner LaserTechnik with a minimum available full-viewing (divergence) angle of 30 degrees were chosen at various wavelengths corresponding to the peak excitation wavelengths of fluorophores enumerated previously in Table 2.

3.2.2 Optical coupling lens system for fiber bundle

Standard achromatic doublet and aspheric objective lenses, Fresnel lenses and reflective and refractive collimators were used to improve collimation of the wide beam output of the LEDs into a narrow beam focused onto the fiber bundle proximal face to improve light coupling.

A 19 mm achromatic doublet was used to collimate the LED light. The magnification of the collimated light size as it passes through the focusing lens is determined by m=$F_{focusing\ lens}/F_{collimating\ lens}$ (where F is the focal length). The second lens was chosen such that the focal length was either the same or smaller than the collimating lens, so that a spot size of the same dimensions as the LED die or smaller was focused onto the fiber bundle. This helps to maximize light focused within the bundle's active area. Hence, an achromatic doublet of the same focal length, Fresnel lenses and aspheric lenses were explored to obtain the best coupling into the fiber. Aspheric lenses maximize the numerical aperture keeping the lens diameter a minimum. Minimization of the spot size on the fiber by choosing a smaller focal length and optimal

matching of the NA of the focusing lens (tube lens) to the fiber NA of 0.33 should improve optical coupling. The results are summarized in Table 3.

Table 3: Focusing lens combinations for optimization of optical coupling into fiber.

Focusing lens, focal length (mm)	Numerical aperture of focusing lens	Power coupled into fiber w/o excitation filter (in mW)
Achromatic doublet, 19 mm	0.33	0.6
Infinity corrected objective lens (Leica, L-10X), 18.2 mm	0.25	0.9
Fresnel Lens, 15 mm	0.85	1.3
Fresnel Lens, 10 mm	0.63	1.49
Aspheric lens, 11 mm	0.25	1.4
Aspheric lens, 8 mm	0.5	1.61
Aspheric lens, 3.1 mm	0.68	0.65
Aspheric lens, 6.24 mm	0.4	1.585
Aspheric lens, 15.4 mm	0.16	0.77
Aspheric lens, 4.5 mm	0.55	1.2

Based on the results, the highest optical coupling obtained is with the 8mm focal length aspheric lens, with a coupling of 1.61 mW without and 1.3 mW with a band-pass excitation filter (1.34 % and 1.1 %, respectively, with the LED output at 120 mW). This is followed by the 6.24 mm focal length aspheric lens with a coupling of 1.585 mW of light (1.32 %). The infinity corrected achromatic doublet (Leica L-10X) was chosen to minimize aberrations and since it had an NA of 0.25 which was very close to the averaged NA of 0.33 for fibers in the entire bundle. This combination provided a power output of 0.9 mW. Further improvements in the coupling will require a delicate removal of the dome lens of the LEDs and the use of smaller focal length collimating lenses so that a narrower beam of light can be focused onto the bundle while keeping the beam NA smaller than the fiber bundle NA. This will help to maximize incoming light that is

internally reflected. Laser light sources can also be employed in place of the LEDs since they have very low beam divergence which can enable the focused beam NA at the fiber tip to be minimized.

3.3 Fiber bundle selection

A Sumitomo IGN-08/30 fiber bundle was used in the *in vitro* and *ex vivo* subcutaneous experiments. A fiber bundle comprising 30,000 individual fibers, with a fiber core- to-core separation specification of 4 μm (the spacing can vary between 3 to 4 μm owing to tolerances in the fiber bundle manufacturing process) was chosen. The selection was performed such that the fibers had the smallest available core-to-core spacing, with the minimum available diameter for multi-mode fibers (~ 3 μm) and had the highest available NA (0.35) for efficient optical coupling. For future *in vivo* endo-tracheal imaging, an appropriate bundle size is essential so that it may fit into conventional endoscopic guides and catheters that are typically employed in animal studies. An endo-tracheal catheter of a specific gauge size can accommodate needle sizes smaller than its inner diameter for intra-tracheal infection of mice. Likewise, fiber bundles smaller than this size can be inserted into these catheters and manipulated freely inside the animal. Bundles of overall diameters in the range of 0.6-0.7 mm can efficiently fit in a 22 gauge catheter, which is typically used in the endo-tracheal infection of mice. Hence, an IGN-05/10 fiber-bundle, comprising 10,000 elements, 4 μm fiber-to-fiber spacing in a 660 μm bundle diameter was ordered for future work.

4. METHODS

Following the design of the system, the characterization of its performance in imaging simple fluorescent samples is essential before moving on to the imaging of fluorescent bacteria, which is the main aim of the study. This is useful in determining the resolution and detection limits of the system. It is also useful in judging whether the system parameters such as excitation power, background and excitation light removal are optimized to obtain quality images. The detection limits of the imaging system at low fluorescence levels similar to those expected from *in vivo* fluorescent bacteria were assessed with this information.

Ex vivo imaging of subcutaneously and intra-tracheally infected mice help to determine the *in vivo* detection capability and system optimization for subsequent *in vivo* imaging of lung tissue. Bacillus Calmette-Guérin (BCG) bacteria, an attenuated form of the live bovine tuberculosis bacillus, *Mycobacterium bovis* and used as a vaccine for *Mycobacterium tuberculosis*, was used in all the experiments. BCG was chosen for the study for safety considerations owing to their non-virulence to humans. The work performed here is approved by the Texas A&M Institutional Animal Care and Use Committee, AUP no. 2008-278.

4.1 System characterization using a resolution target and fluorescent dye stained samples

The system was first set in reflectance mode for imaging the reflectance resolution target and then to fluorescence mode for imaging the dye stained samples.

4.1.1 Resolution target imaging

A 1951 USAF resolution target (Edmund optics, NT38-256) was imaged by contacting the fiber bundle onto the reflectance target and finding the smallest discernible line pairs as well as the lines pairs that have distinctly separable pairs. This information, which is available in lines per mm is then inverted and halved to determine the minimum line width that can be resolved by the system.

4.1.2 Fluorescent sample imaging

Common fluorescent dyes such as acridine orange and fluorescein were prepared in standard concentrations (1 mg/mL), and imaging was performed by directly placing the probe into the liquid media. The fluorescent light output was then quantified by analyzing the images taken by the camera via the ImageJ software. Concentrations were subsequently diluted to test the detection limit of the camera.

1 mg/mL concentrations of the DNA intercalating dye, acridine orange was used to stain the nuclei of tissue samples of hamster cheek pouches acquired through tissue sharing (Dr. Brian Applegate's cancer study at Texas A&M University) to assess the cellular and tissue resolution capabilities of the system. Staining was performed by soaking the samples in the dye for approximately 10 minutes. This was followed by washing with phosphate buffer solution to clear off excess un-reacted dye.

4.2 *In vitro* imaging of fluorescent bacterial colonies

Bacteria expressing various proteins such as green fluorescent protein (GFP), tdTomato, mKeima and mCherry were grown in colonies on agar as well as in suspension in culture medium. The probe was placed in contact with the *in vitro* sample

and the fluorescent signal from the bacteria was collected by the fiber bundle and imaged onto the CCD. This information was then used to characterize the sensitivity for bacteria expressing different fluorescent proteins in order to select the optimal fluorescent protein for subsequent *ex vivo* experiments on excised tissue from infected animals. Although individual bacteria were not expected to be resolved by the imaging system, ability to resolve bacterial colonies may indicate sufficient capability to image regions of bacterial infection *ex vivo* as well as *in vivo*.

4.3 *Ex vivo* imaging of mice subcutaneously infected with fluorescent bacteria

Subcutaneous injection of a bolus of bacteria provides a localized population of a known concentration in an accessible location for a simple test of the imaging system's capability to detect and image regions of bacterial infection. Six mice were divided into two groups that were anesthetized and injected with 50 μL of three different concentrations of tdTomato expressing bacteria subcutaneously. Each animal was injected with a negative control sample. The first group was injected with 10^6, 10^5 and 10^4 colony forming units (CFU) while the second group was injected with 10^3, 10^2 and 10^1 CFU. Imaging was performed one day following infection, using the appropriate excitation and emission filters for tdTomato.

The mice were euthanized and excoriated in the infection zone and imaging was performed from the underside of the skin (Figure 8 A). For each imaging site, in three regions where a definite signal was obtained, a biopsy was carried out with a 1 mm punch biopsy needle (Miltex sterile disposal with plunger, Figure 8 B). Three negative control sites per concentration were also imaged and biopsied.

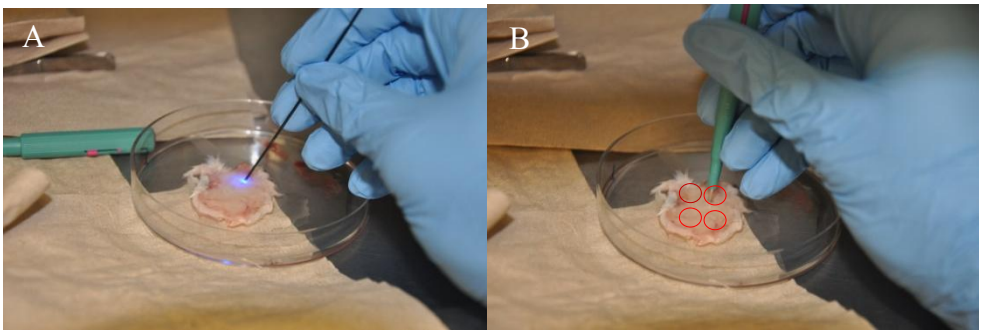

Figure 8: A) *ex vivo* imaging of excoriated subcutaneous tissue; B) biopsy samples being taken from excoriated subcutaneous tissue; circles depict injection sites.

These biopsy samples were then transferred to a growth medium and subsequently incubated for a period of three weeks for CFU count measurements. Separate biopsies of confirmed infection sites were also taken for a histo-pathological investigation. The fiber-bundle fluorescence signal was quantified for the three regions of different concentration and the control to validate the experiment. This data will then be compared with the biopsy CFU count to analyze the correlation between the two.

4.4 *Ex vivo* imaging of excised lung tissue from intra-tracheally infected mice

Imaging of excised lung tissue allows determination of the sensitivity of the system to image bacteria within lung tissue and characterization of the probable locations of bacteria within the respiratory system following intra-tracheal infection. In addition to improved access to the lung tissue in comparison to *in vivo* lung imaging, *ex vivo* imaging circumvents size restrictions imposed on the probe during *in vivo* imaging. A catheter was inserted into the trachea of the six previously anesthetized mice (common to the subcutaneous experiments). A bolus containing 10^6 CFU fluorescent bacteria each for five mice, and 10^6 CFU of a non-fluorescent control in the sixth mouse was then

administered. A day was allowed post injection of bacteria into the respiratory system of the mice, to permit bacteria to reach deeper regions of the lungs. The mice were then euthanized and their lung tissues were excised. Imaging was performed at various sites (trachea and bronchi) to identify the regions with the maximum fluorescence signal. This will aid in anticipation of regions of early infection for guidance of probe placement during future *in vivo* lung imaging.

5. RESULTS

5.1 System characterization

5.1.1 Imaging of Air Force resolution target

A 1951 USAF resolution target was imaged using the system to confirm the theoretical resolution and field-of-view values determined by the fiber bundle specifications. As shown in the reflectance image of the resolution target (Figure 9 A), group 6, element 4 is clearly visible and the last group that is barely discernible is group 7, element 2 (blow-up shown in Figure 9 B).

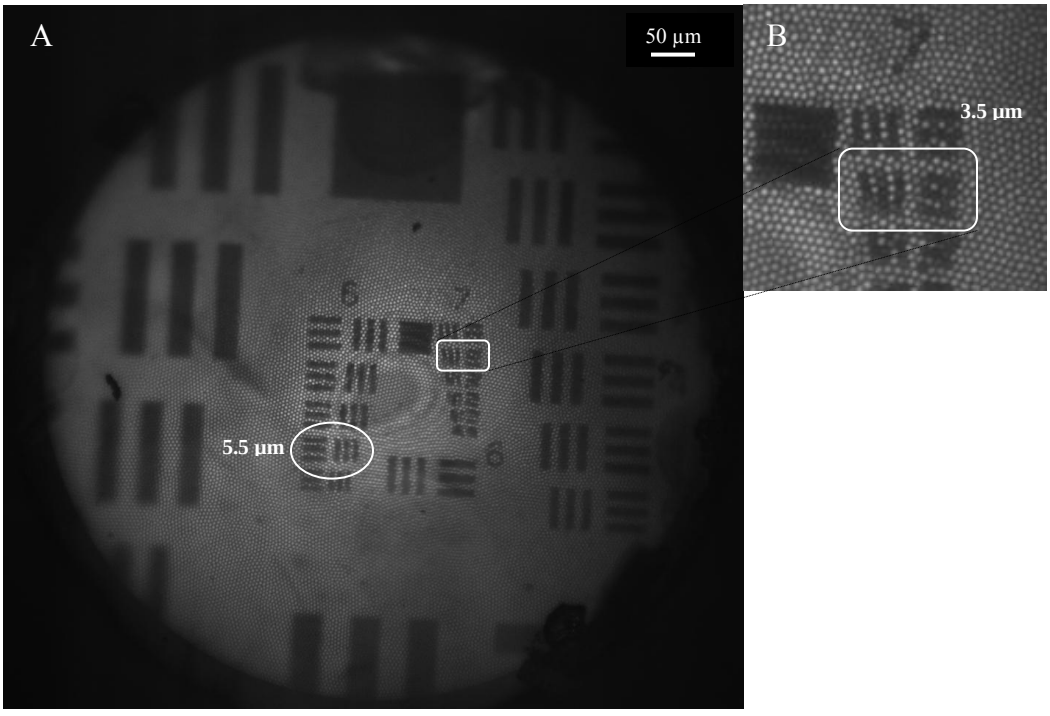

Figure 9: A) Reflectance image of Air-force resolution target; B) blow-up of group 7, element 2.

According to the Edmund Optics specification charts [35], Group 6, element 4 has 90.5 lines pairs per mm corresponding to 5.5 μm/line width. Group 7, element 2 has 144 lines pairs per mm, corresponding to a 3.5 μm resolution. Therefore, the system can clearly distinguish features down to 5.5 μm and the point beyond which there is difficulty in distinguishing between different lines corresponds to resolution limit of 3.5 μm. This value agrees with the limit established earlier corresponding to the fiber core-to-core spacing that has a manufacturing specification of 4 μm but can vary between 3 to 4 μm.

5.1.2 Demonstration of cellular and tissue level resolution

The cellular and tissue level resolution of the system was determined via the imaging of 15 μm fluorescent microspheres and nucleic acid-fluorescence stained hamster cheek epithelial cells.

15 μm Dye-Trak fluorescent microspheres were injected into a PBS solution to create a fluorescent microsphere suspension. This was then imaged by placing the fiber-bundle inside the PBS solution. As can be seen from the image in Figure 10, those microspheres which are in contact with the probe are clearly visible as a pixilated image (corresponding to the superposition of the bundle structure on the microsphere image). Microspheres that are not physically in contact with the bundle are visible as blurred spots with lower intensity.

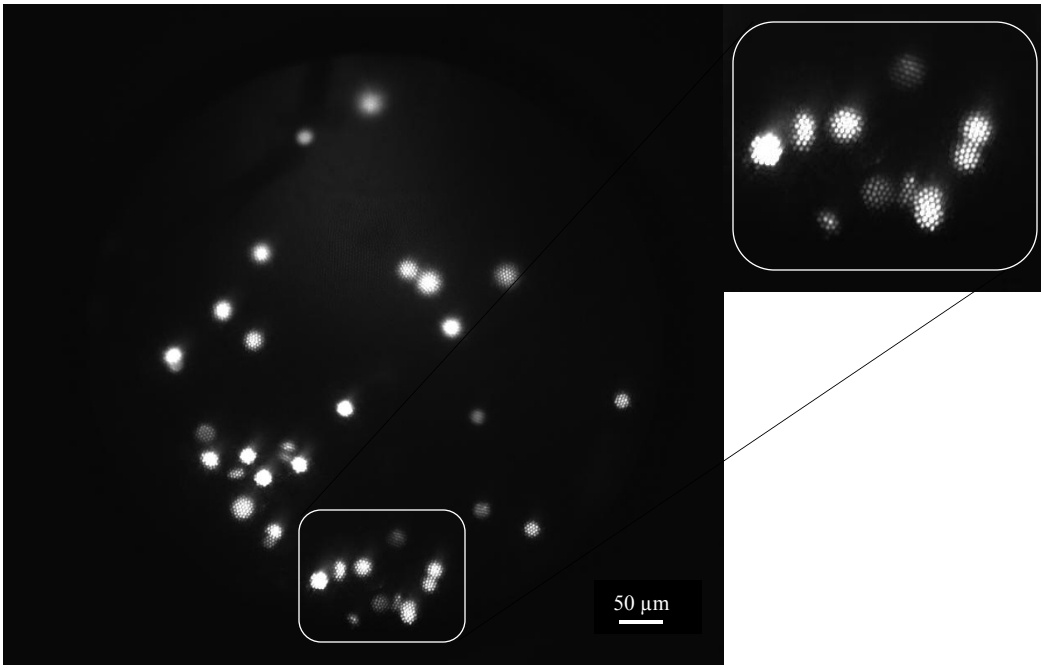

Figure 10: A) Dye-Trak yellow 15 µm fluorescent microspheres; B) blow-up of image region showing individual microspheres.

The tissue of the hamster cheek pouch stained with fluorescent dye was imaged. The nuclei stained by the acridine orange are clearly visible as seen from the encircled example from the image in Figure 11. The system gave well resolved images of hamster cheek pouch cells (typically 10 µm in diameter). This suggests that the system is capable of resolving typical cellular and tissue level features.

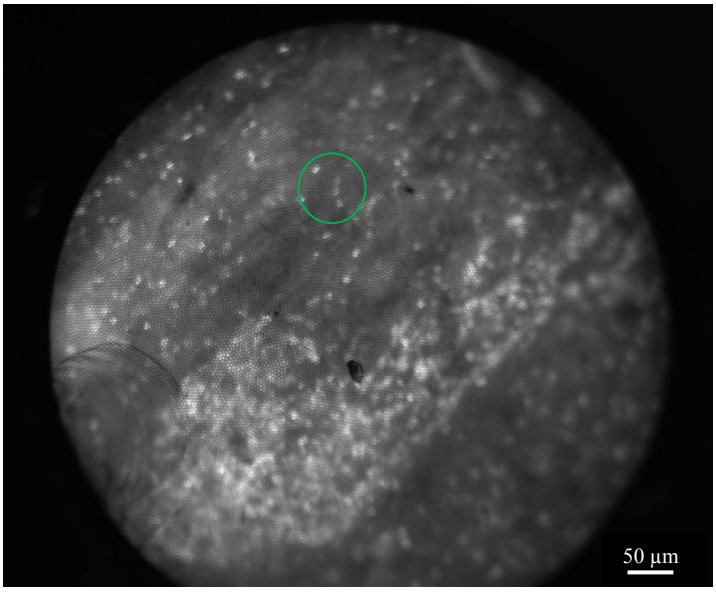

Figure 11: Hamster cheek epithelial cells stained with acridine orange.

5.2 *In vitro* imaging of GFP-actin expressing cells

GFP-actin expressing osteoblast cells (provided by Dr. Roland Kaunas, Texas A&M University) grown *in vitro*, were imaged on a petri-dish as shown in Figure 12, at an exposure of 780 msec and a gain setting of 7. The images show well resolved osteoblast cell structure that demonstrates the cellular resolution capability of the system. In addition, these results demonstrate promise for future dual-channel imaging of GFP expressing cells infected by tdTomato expressing bacteria.

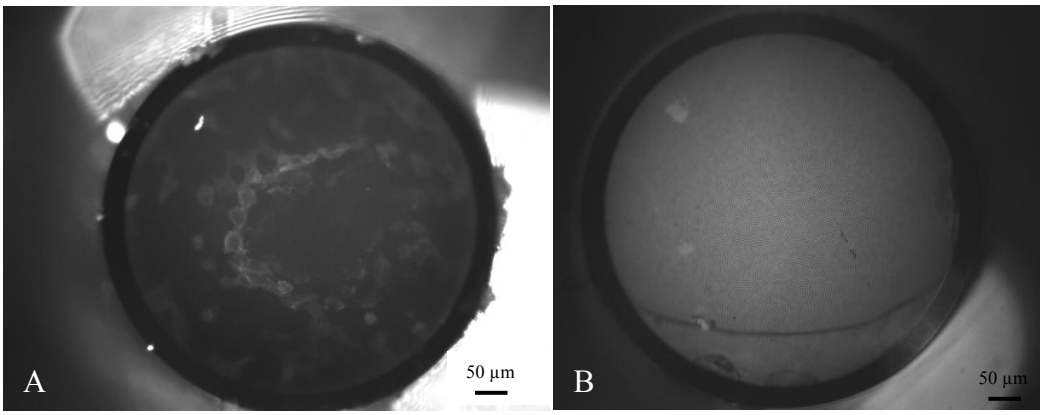

Figure 12 : A) GFP actin expressing cells grown *in vitro*; B) *in vitro* negative control.

5.3 *In vitro* imaging of bacterial samples

To assess the sensitivity of the system to image bacteria expressing different proteins, fluorescent strains of bacteria were imaged *in vitro*. Images of tdTomato and GFP expressing bacterial colonies grown on agar were successfully obtained *in vitro* as shown in Figures 13 A and B. Based on the signal and resolution, these images indicate that both GFP and tdTomato expressing bacterial colonies can be detected and well resolved *in vitro*, in comparison to the negative control (non-fluorescent BCG with vector backbone, Figure 13 C). We hence expect GFP and tdTomato expressing regions of bacterial infection to be detectable *in* vivo. The tdTomato protein has a higher quantum yield than enhanced GFP (0.69 as compared to 0.6 for the EGFP, [36]) and a brightness (product of quantum yield and extinction coefficient) that is 2.8 times higher than EGFP [37]. Being a red-shifted protein, tdTomato emits in the 580 to 700 nm range, where there is a steep drop in the light absorption owing to hemoglobin in tissue [38]. Moreover, tissue auto-fluorescence is reduced at higher wavelengths. Therefore tdTomato expressing bacteria were chosen for our subsequent experiments.

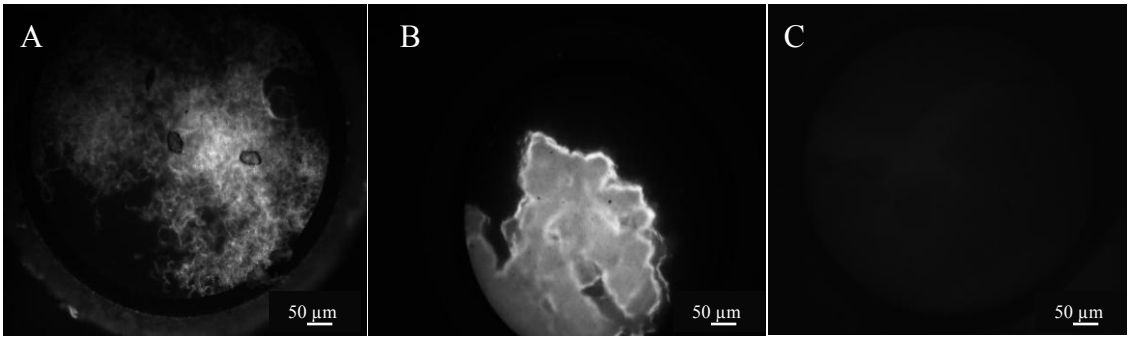

Figure 13: A) GFP expressing bacterial colonies grown on agar; B) tdTomato expressing bacterial colonies grown on agar; C) negative control on agar (non-fluorescent BCG bacteria with vector backbone)

5.4 *Ex vivo* imaging of subcutaneously infected mice tissue

Subcutaneously injected tdTomato expressing bacteria at concentrations varying from 10^6 to 10^1 CFU were then imaged *ex vivo* as shown in Figures 14, 15 and 16 (all images presented were contrast enhanced by 72 % and brightness enhanced by 50 %). The corresponding macroscopic image taken with the IVIS Spectrum system is shown in Figure 14F. Sites inoculated with 10^6 CFU (Figures 14 A and B) and 10^5 CFU (Figures 14 C and D), clearly show well resolved bacterial infection foci (regions encircled green) in comparison to the 10^6 CFU of non-fluorescent negative control bacteria (Figure 14 E), which displays only background auto-fluorescence. This is also corroborated with the macroscopic IVIS system image.

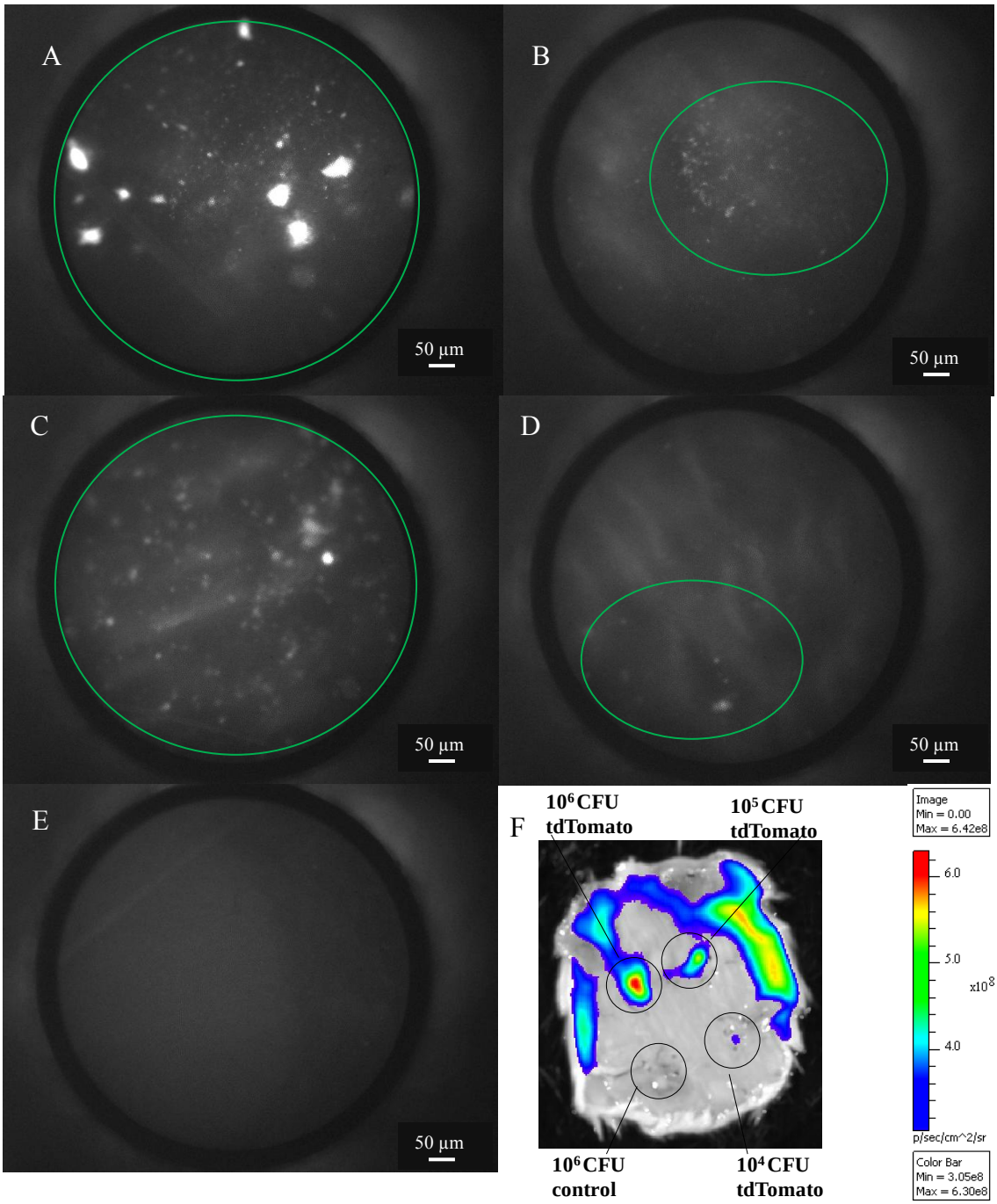

Figure 14: tdTomato expressing bacteria injected subcutaneously at various concentrations: A) and B) 10^6 CFU; C) and D) 10^5 CFU; E) 10^6 CFU of non-fluorescent bacteria (negative control); F) macroscopic IVIS image of subcutaneously infected tissue.

Bacterial concentrations down to 10^4 CFU (Figures 15 A and B) are clearly detected in comparison to the negative controls (Figures 15 E and F) and corroborated with the IVIS images, which did not give any signal for inocula below 10^3 CFU. For the lower bacterial concentrations, 10^3 CFU (Figure 15 C and D), 10^2 CFU (Figures 16 A and B) and 10^1 CFU (Figures 16 C and D), there appears to be ambiguity in determining, whether the fluorescence signal is from bacteria that are attached or associated with fibrous auto-fluorescent structures or are from topological features in the structures themselves. For instance, in Figure 15 D, bacteria (encircled green, lower left), appear to be attached to the fibrous structure; while in Figure 15 C, it isn't clear whether the bright spots (encircled blue) associated with the fibers are bacteria or part of the surrounding anatomical features. The inoculation dose from 10^1 CFU to 10^6 CFU appears to correlate with the size of the bacterial infection foci.

There seems to be site to site variability within the same bacterial concentration as is visible from the comparison of Figures 14 A and B for an inoculum of 10^6 CFU and 14 C and D for an inoculum of 10^5 CFU. Background auto-fluorescence between samples also varies, as can be seen from the auto-fluorescent fibrous structures seen in the negative control images in Figures 15 E and F. This variability can also be seen between the images of the 10^1 CFU bacterial concentration and negative control, the 10^1 CFU sample having lower auto-fluorescence than the negative control (Figures 16 C and F respectively).

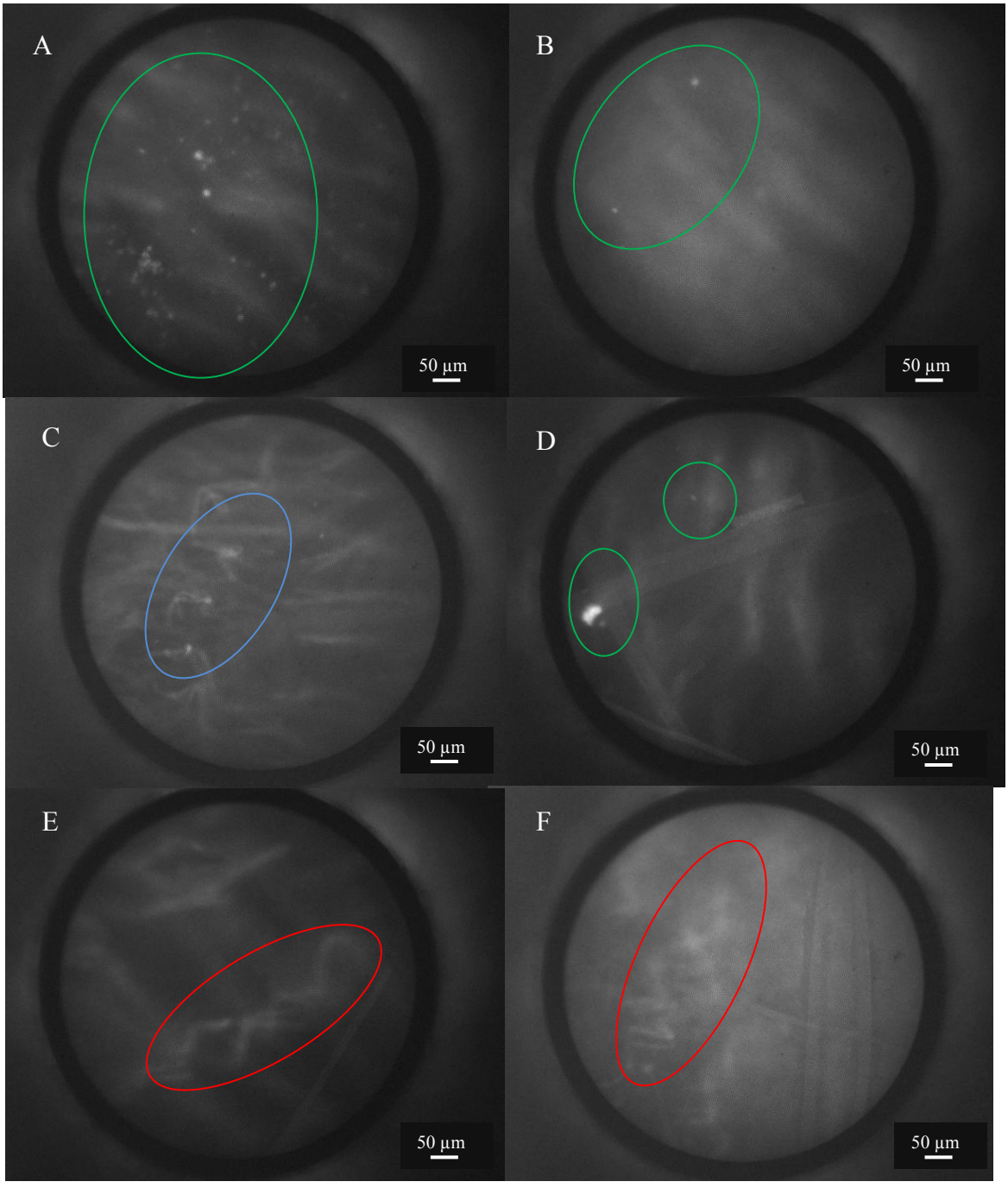

Figure 15: tdTomato expressing bacteria injected subcutaneously at various concentrations: A) and B) 10^4 CFU; C) and D) 10^3 CFU; E) and F) 10^6 CFU of non-fluorescent bacteria (negative controls).

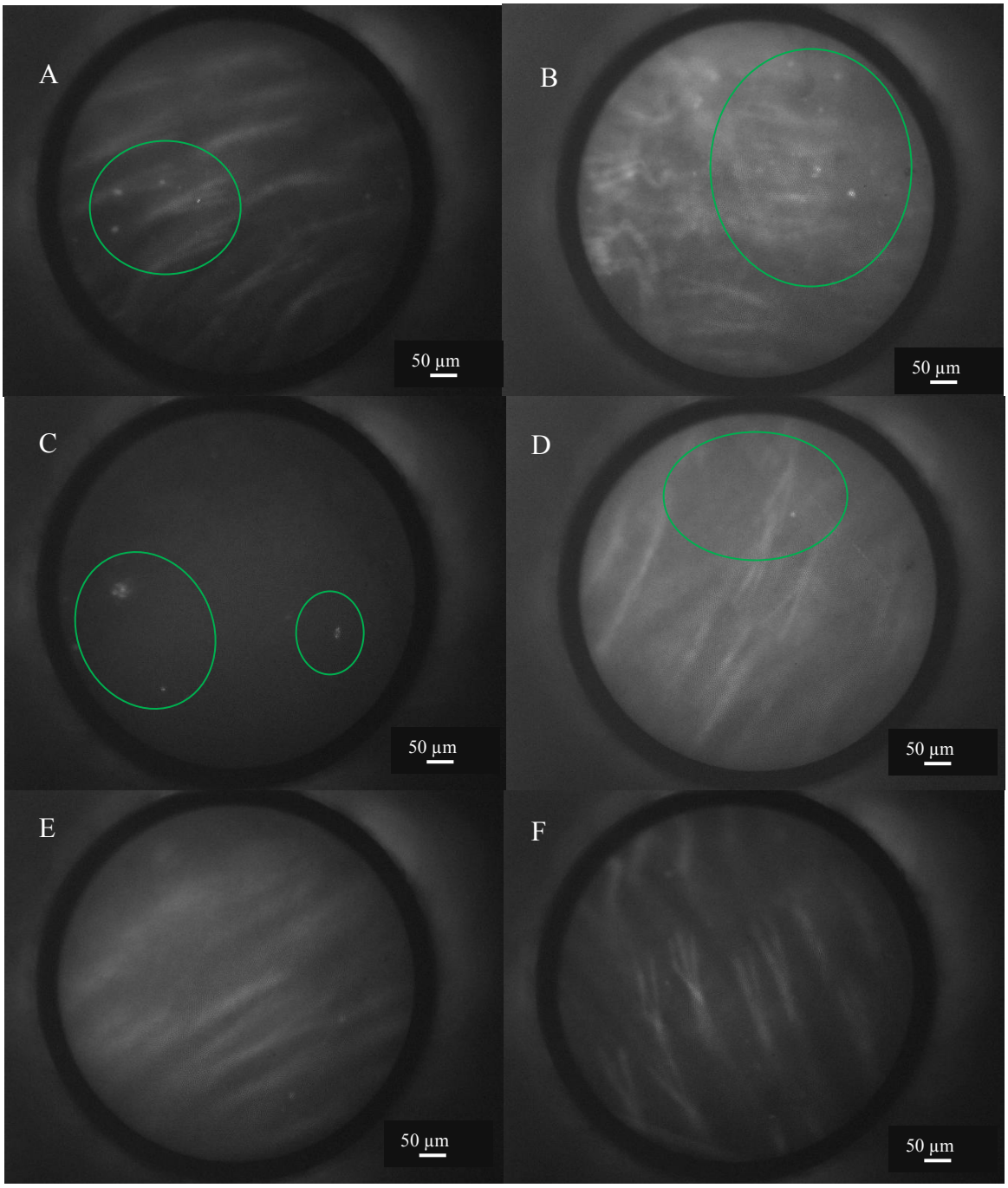

Figure 16: tdTomato expressing bacteria injected subcutaneously at various concentrations: A) and B) 10^2 CFU; C) and D) 10^1 CFU; E) and F) 10^6 CFU of non-fluorescent bacteria (negative controls).

5.5 *Ex vivo* imaging of lung tissue infected intra-tracheally with 10^6 CFU of bacteria

Following the success of the subcutaneous imaging, the lungs of the mice were excised and imaged *ex vivo.* Figures 17 A and B display regions of fluorescent bacterial infection in the lung tissue as compared to mice inoculated intra-tracheally with non-fluorescent bacteria as seen in Figure 17 C. The corresponding macroscopic images obtained with the IVIS are shown in Figure 17 D. The 10^6 CFU fluorescent bacteria inoculum images in Figures 17 A and B clearly show detectable regions of bacterial infection (encircled green) as compared to the negative controls in Figure 17 C. The fluorescence images again corroborate those obtained from the IVIS. Variability in the size of the regions of infection in figures 17 A and B is again visible.

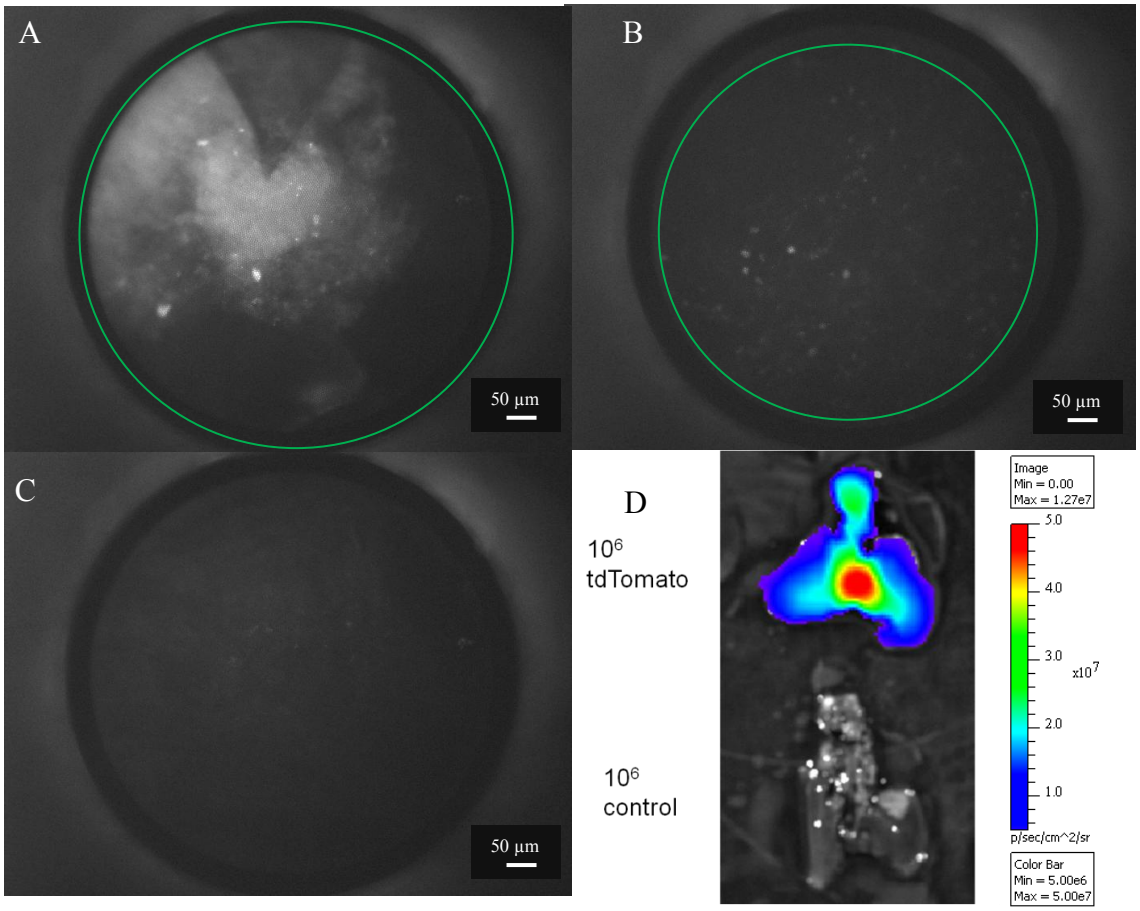

Figure 17: tdTomato expressing bacteria injected intra-tracheally into the lungs of mice at 10^6 CFU (A) and (B); (C) 10^6 CFU of non-fluorescent bacteria injected intra-tracheally into the lungs (negative control); (D) macroscopic IVIS image of 10^6 CFU intra-tracheal inoculum of fluorescent bacteria.

6. DISCUSSION

6.1 Analysis of images

The characterization studies show that features down to 4 μm are clearly visible, as seen in the resolution target image (Figure 9). Moreover, the well resolved images of the 15 μm microspheres (Figure 10), as well as the 10 μm hamster cheek cells (Figure 11), demonstrate the cellular and tissue level resolution of the system. Human cells in comparison are 1-10 μm in size, with the nuclei being typically less than 5 μm.

These results are corroborated by *in vitro* imaging of GFP actin expressing cells (Figures 12 A and B) and bacterial colonies expressing fluorescent proteins (Figures 13 A and B). These data show that both tdTomato and GFP expressing BCG bacteria can be detected and resolved. This further indicates that the system is capable of detecting bacteria in *ex vivo* and *in vivo* samples. No structural information could be obtained from bacterial colonies expressing mCherry and mKeima, perhaps because the system's filters were not optimized for those wavelengths. The tdTomato protein has a higher quantum yield (0.69 as compared to less than 0.6 for EGFP [36]), and a brightness (product of quantum yield and extinction coefficient) that is 2.8 times that of EGFP [37] and the highest for the red-shifted proteins. tdTomato emits in the 580 to 700 nm range, where there is a steep drop in the light absorption owing to hemoglobin in tissue [38]. Furthermore, tdTomato expressing cells have been shown to provide higher detection sensitivity for *in vivo* optical imaging applications as compared to EGFP [10]. It was therefore selected as the fluorescent protein of choice for the rest of the experiments.

Although imaging bacteria in the lung is the ultimate goal, imaging bacteria of concentrations from 10^6 to 10^1 CFU subcutaneously injected in the skin of mice provides well controlled conditions and ease of accessibility for characterizing sensitivity in tissue. Since the imaging probe can, at present, only image areas that are in contact with bundle-tip, owing to limited optical penetration depth in tissue, the mice were excoriated to expose the underside of the skin for direct imaging of the infection site. Comparing the imaging results in Figures 14 A and B (10^6 CFU) as well as 14 C and D (10^5 CFU) with the negative control in Figure 14 E, we find clearly detectable regions of bacterial infection. This also corroborates with the regions of infection indicated by macroscopic imaging IVIS Spectrum (Figure 14 F). Detectable regions of bacterial infection can also be seen at concentrations down to 10^4 as is visible in Figures 15 A and B. There is ambiguity in the detection of regions of infection for the lower inoculums, 10^3 CFU (Figure 15 C and D), 10^2 CFU (Figures 16 A and B) and 10^1 CFU (Figures 16 C and D) in comparison to the negative controls (Figure 15 E and F and Figures 16 E and F). The size of the infection foci within the field of view seem to correlate with the inoculum.

However, as can be seen from a comparison of images Figures 14 A and B as well as Figures 15 A and B, there is variability in the size of the regions of infection between different imaging sites with the same inoculum. It is possible that there is heterogeneity in the distribution of bacteria after injection into the tissue owing to the dynamics of the inoculum fluid flow in the subcutaneous tissue. Since the probe's field-of-view is much smaller than the region of inoculation and infection, we may not necessarily be imaging the same concentration as the inoculum. This variation between

imaging sites may also be explained by an 'infection' diffusion gradient that is visible in the macroscopic IVIS system image (Figure 14 F) as a region of decreasing bacterial concentration that spreads outward from the point of injection. This phenomenon could be due to the dynamics of the inoculum fluid flow in the subcutaneous tissue as well as cellular uptake rates during phagocytosis and how that is influenced by variation in inoculum concentration. It is possible that when imaging two different sites close together, zones of different levels of infection may be touched upon and hence a different fluorescence signal will result. These theories may also apply to images obtained from two different concentrations displaying regions of infection having the same size as can be seen from Figures 15 B (10^4 CFU) as compared to 16 C (10^1 CFU).

The variability in the auto-fluorescence background signal as displayed in Figures 15 E and F (negative controls) as well as between Figures 16 C and F (10^1 CFU and negative control, respectively) could be due to the presence and variation of fiber like structures which contribute to the auto-fluorescence. Bacteria also appear to aggregate or associate with some of these auto-fluorescent fiber structures as seen in Figure 15 D. The ambiguity associated with some of the images appearing to be either regions of bacterial infection, or anatomical features within the tissue structure, should become clear following a CFU count measurement and after analysis of histopathology information from the site biopsies.

Images of *ex vivo* lung tissue, Figures 17 A and B, indicate that definite regions of fluorescent bacterial infection can be detected in lung tissue as compared to excised lung tissue infected with 10^6 CFU of non-fluorescent bacteria (Figure 17 C). These

images correlate well with the corresponding regions shown in the macroscopic images taken with the IVIS system (Figure 17 D). Bifurcation points in the trachea were seen to typically have a larger number of bacteria. Fluorescence from deeper regions of the lungs was also detected, which could be attributed to the respiration of the mouse as well as normal physiological processes such as drainage of bacteria via the lymphatic system.

These results show promise for this device to be used for *in vivo* imaging of regions of bacterial infection inside the lungs of animals by delivering the fiber probe to the site of infection using a catheter. This approach can be used to assist whole body imaging systems in identifying and imaging regions of infection at a higher resolution so as to perform time-studies of physiological processes such as phagocytosis. Initially, *in vivo* imaging of higher inoculation doses may be guided by whole body fluorescence imaging scanners. Eventually regions of infection at concentrations lower than the detection limit for macroscopic imaging systems may also be accurately imaged.

6.2 Image quantification and evaluation of the limit of detection

6.2.1 Image quantification

To assess the variation in the fluorescence intensity with increasing inoculum dose and variation within the fluorescence intensities of each individual inoculum, the fluorescence intensity of each image obtained was averaged over all the pixels. The scatter plot of the average fluorescence intensity from the negative control and each inoculum dose was plotted against the inoculum dose on a log scale as shown in Figure 18. The mean fluorescence intensity at each inoculum versus the inoculum dose was plotted as shown in Figure 19.

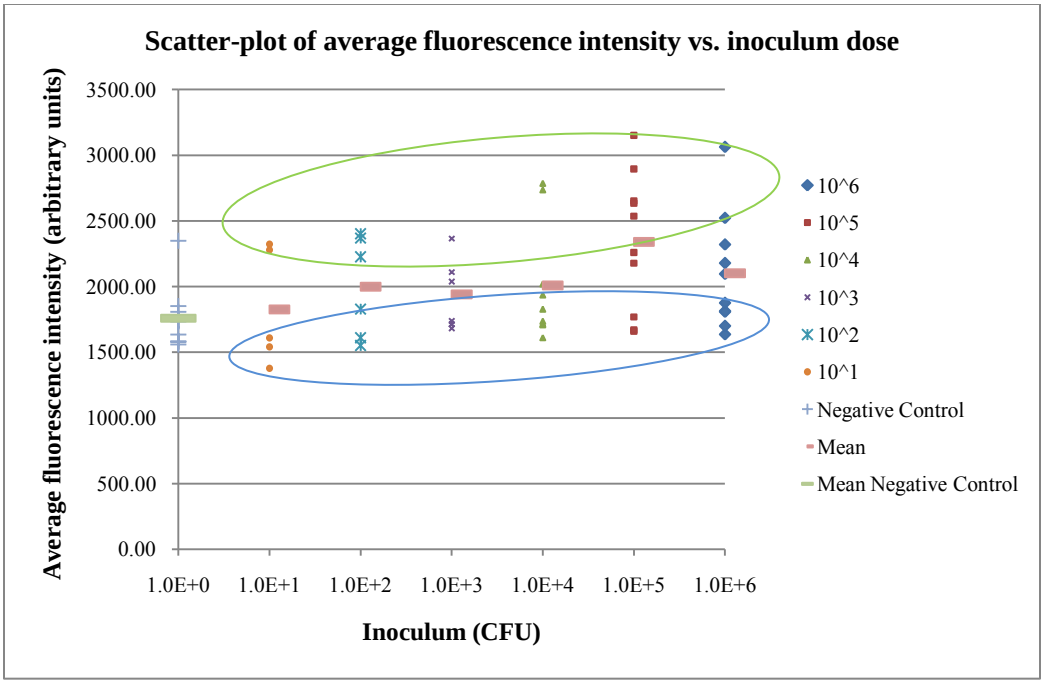

Figure 18: Scatter-plot of average fluorescence intensity over the probe's field-of-view vs. subcutaneous fluorescent bacterial inoculum.

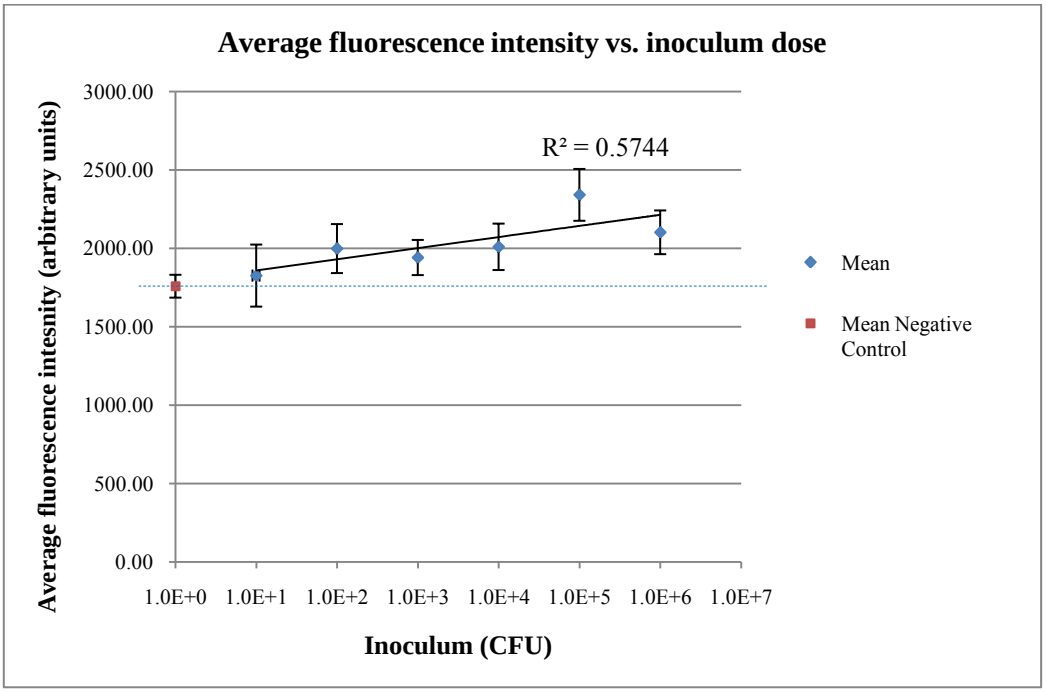

Figure 19: Average fluorescence intensity over the probe's field of view vs. subcutaneous fluorescent bacterial inoculum.

As can be seen from the scatter plot in Figure 18, an increasing trend is seen in the average fluorescence intensity with increasing inoculum levels. Additionally, a bi-modal distribution is seen for the average fluorescence at each inoculum, with a group of low values (encircled blue) and high values (encircled green). This can be explained from the fact that when the probe is placed in contact with a subcutaneous infection zone, due to the heterogeneity in the local distribution of the bacteria within the field of view of the probe, very low as well as higher, more representative levels of bacteria for each inoculum are sampled. This can be seen for every inoculum dose as groups of low and high fluorescence intensity measurements.

An increasing trend is seen in the average fluorescence intensity with increasing inoculum dose till 10^5CFU beyond which there seems to be saturation in the bacterial load that a tissue sample within the field-of-view can hold.

A correlation between the average fluorescence intensity and the subcutaneous inoculum dose was then performed as seen in Figure 19. The logarithmic regression fit to the data (with an R^2 value of 0.57), again displays an increasing trend, with the mean fluorescence of all inocula above 10^2 CFU being above the negative-control's mean level. The presence of a good correlation would be advantageous in determining a calibration curve for the system so as to enable rapid quantification of regions of fluorescent bacterial infection.

6.2.2 Statistical evaluation of the limit of detection using Student's t-test

To determine the detection limit of the system, a statistical analysis of the average fluorescence vs. inoculum data was performed using Statgraphics Centurion®.

A Box-and-Whisker plot (Figure 20) for the entire data set was performed to evaluate the variation in the fluorescence intensity with increasing inoculum dose and within the same inoculum. As was noted earlier, the mean levels (red square) of the fluorescence intensities at each fluorescent bacterial inoculum are higher than that for the negative control. There is an overlap in the intensities for the 10^1 CFU and 10^2 CFU inocula with the negative control data.

To accurately compare the means of each of the fluorescence intensities with the negative control, and to determine which inoculum dose has a statistically significant difference in its mean fluorescence as compared to that of the negative control, a Student's t-test was performed for each of the negative control-fluorescent inoculum dose pairs. A descriptive example for the comparison of the fluorescence intensities of the negative-control vs. 10^2 CFU is provided.

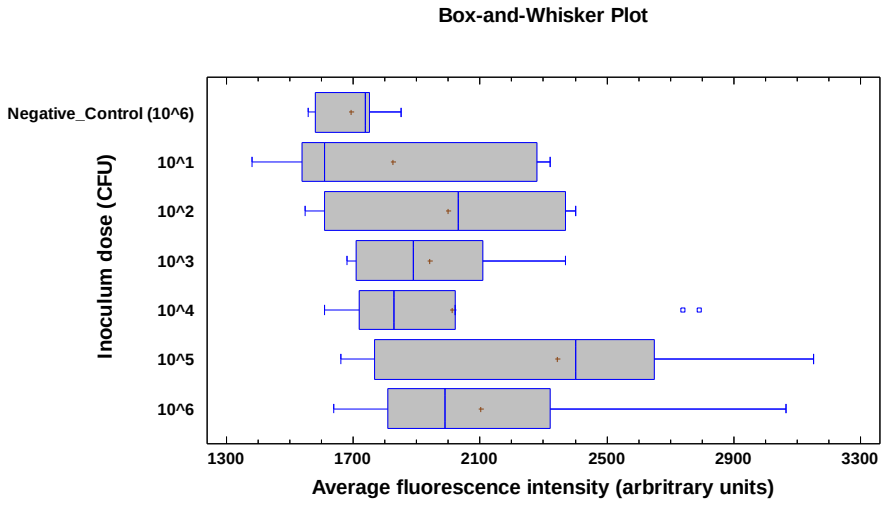

Figure 20: A Box-and-Whisker plot of the average fluorescence intensity vs. subcutaneous inoculum dose.

The 95.0% confidence interval for the mean fluorescence intensity from the negative control was determined to be 1693.33 ± 82.9665 (ranging from 1610.37 to 1776.3). The 95.0% confidence interval for the mean fluorescence intensity obtained from the 10^2 CFU inoculum was determined to be 1998.33 ± 401.891 (ranging from 1596.44 to 2400.22) and that for the difference between these two assuming equal variances was -305.0 ± 287.093 (ranging from -592.093 to -17.9068). Since this range does not contain the value 0, it indicates that there is a statistically significant difference between the two means at the 95 % confidence interval.

The null hypothesis states that the mean for the fluorescence intensities obtained for the negative control and each inoculum dose compared to it are equal. The alternate hypothesis states that they are not equal. Assuming equal variances, we obtain a p-value of 0.039 for the t-test between the negative control and 10^2 CFU data. Since the p-value is lower than 0.05, we can hence reject the null-hypothesis in favor of the alternate hypothesis. There is hence a statistically significant difference between the mean fluorescence obtained from the negative control samples in comparison to that obtained from the 10^2 CFU inoculum. The p-values for the negative control and each of the higher inoculum doses are also lower than 0.05 (with the exception of the 10^4 inoculum data with a close p-value of 0.054). Performing the t-test for the negative control and the lower inoculum of 10^1 CFU, we get a p-value of 0.39. Since this is greater than 0.05, we cannot reject the null hypothesis and hence there is not a statistically significant difference between the two samples. The p-values for the comparison between the negative-control and the various inocula are summarized in Table 4. Since the lowest

inoculum dose that has a p-value lower than 0.05 when compared to the negative control is 10^2 CFU, the detection limit for the system is determined to be 10^2 CFU.

From a statistical point of view, the system is be able to detect bacteria down to 10^2 CFU. Based on the earlier mentioned ambiguity in the images taken for the inoculums lower than 10^4 CFU, the presence of bacteria in lower inocula will have to be verified via CFU measurements.

Table 4: P-values for a Student's t-test comparison of the mean fluorescence intensity obtained from 10^6 CFU of negative control with various subcutaneous inocula of fluorescent bacteria.

Fluorescent bacteria inoculum (CFU)	P-value for mean fluorescence comparison of inoculum with 10^6 CFU of negative control
10^1	0.395
10^2	0.039
10^3	0.029
10^4	0.054
10^5	0.002
10^6	0.015

7. CONCLUSIONS AND FUTURE WORK

A fluorescent micro-endoscope with a resolution of 4 μm and a field of view of 750 μm diameter was developed. System characterization using a resolution target confirmed that features of 5.5 μm were clearly visible and a resolution limit of 3.5 μm was possible. Moreover, *in vitro* imaging of 15 μm fluorescent microspheres, dye stained hamster cheek cells and GFP-actin expressing osteoblast cells demonstrated the cellular and tissue level resolution of the system.

In vitro imaging of tdTomato and GFP expressing bacteria showed that the system could detect and resolve bacteria and *ex vivo* imaging of mice subcutaneously infected with tdTomato expressing cells confirmed similar imaging capabilities at the tissue level. Well resolved regions of bacterial infection were visible at the higher subcutaneous bacterial inoculum concentrations (10^6 and 10^5 CFU) as compared to the negative controls that display only background auto-fluorescence. In addition, bacteria at concentrations down to 10^4 CFU could also be detected and distinguished from background auto-fluorescence. These bacterial infection site images agree with the macroscopic images taken with the IVIS system and display signal at concentrations lower than 10^3 CFU where the IVIS did not register bacteria.

As explained earlier, the site to site variation in the size of the region of infection for the same inoculum may be attributed to heterogeneity in the bacterial concentration and the smaller size of the probe's field of view as compared to the region of infection. This observation may also be due to interplay between the concentration gradient

centered at the injection site and bacterial drainage via the lymphatic system. This is further seen in the bi-modal distribution visible in the scatter plot of the average fluorescence intensity vs. inoculum in Figure 18, where both low and high fluorescence intensities are seen for each inoculum.

Based on the statistical analysis of the quantified images, the system's limit of detection was determined to be 10^2 CFU. It is hence possible that bacteria were also detected at inocula down to 10^2 CFU. Ambiguity in bacterial detection that might be confused with anatomical features present in the auto-fluorescence for inocula lower than 10^4 CFU will have to be cleared up by examining the histo-pathology images and CFU determination from the biopsies.

The fluorescence signal from the bacteria in the images seems to correlate with the inoculum dose, and this is confirmed with the increasing trend seen in the scatter plots for the average fluorescence vs. inoculum dose (Figure 18) and the regression fit for the mean fluorescence vs. inoculum dose (Figure 19). The auto-fluorescence background is not constant and it remains to be seen if it can cause any issues with a correlation between the fluorescence signal and the CFU counts.

An important step forward will be to optimize the excitation wavelengths using suitable band-pass filters and dichroic mirrors so that the fluorescence emission from tdTomato is maximized and tissue auto-fluorescence is minimized. Suitable emission filters employing narrow bands in place of long pass filters will also be explored to reduce the auto-fluorescence background and improve the signal-to-noise (SNR) ratio.

To improve the quantitative aspects of the system in imaging regions of bacterial infection using the system, it would be beneficial to have a mechanism to either minimize or remove the auto-fluorescence. This can be done by performing spectral un-mixing of the imaging data to remove wavelengths corresponding to the emission characteristics of the tissue auto-fluorescence. A system modification that can also enable this could be a replacement of the fixed emission filters with liquid crystal tunable filters (LCTF) which change their pass-bands on the application of electrical current. By analyzing the emission characteristics of the auto-fluorescence structures at various wavelengths for each pixel of the image and comparing it with the emission characteristics of the fluorophore used (tdTomato), the auto-fluorescence signal can be removed via linear subtraction from the image. Spectral-unmixing can also be useful in separating out the fluorescence signal from GFP cells and tdTomato cells in order to visualize/quantify them separately without having to add another imaging channel to the existing system. Another option can be to replace the existing high resolution camera with a hyper-spectral or multi-spectral camera (in which the key component is again the LCTF), which are generally bundled with propriety spectral un-mixing software. Auto-fluorescence can also be minimized by switching to a bioluminescence strategy. By using bacteria or cells that are bioluminescent instead of fluorescent, the SNR can be maximized by reducing auto-fluorescence caused by the excitation light.

Another key improvement that we aim to implement is to modify the system to enable 2-channel imaging of GFP and tdTomato. This will allow dual imaging of GFP expressing cells in mice being invaded by tdTomato expressing bacteria as well as

investigation of the types of cells that phagocytose bacteria with their corresponding dynamics. This can go a long way in visualizing and explaining the physiological spread of bacteria at low inoculum concentrations from the lungs into pulmonary and extra-pulmonary regions, the details of which are not presently well understood.

REFERENCES

1. "Centers for Disease Control, Tuberculosis (tb) Statistics," *http://www.cdc.gov/tb/statistics/default.htm*, July 1, 2010).
2. K. Todar. "Todar's Online Textbook of Bacteriology," *www.textbookofbacteriology.net/tuberculosis.html* (July 21, 2010).
3. J. Kim, D. Byun, M.G. Mauk, and H.H. Bau, "A disposable, self-contained pcr chip," Lab on a Chip **9**(4), 606-612 (2009).
4. H. Wiesinger-Mayr, K. Vierlinger, R. Pichler, A. Kriegner, A.M. Hirschl, E. Presterl, L. Bodrossy, and C. Noehammer, "Identification of human pathogens isolated from blood using microarray hybridisation and signal pattern recognition," BMC Microbiology **7**, 78-94 (2007).
5. Y. Yamamoto, "Pcr in diagnosis of infection: Detection of bacteria in cerebrospinal fluids," Clinical and Diagnostic Laboratory Immunology **9**(3), 508-514 (2002).
6. P. Apfalter, F. Blasi, J. Boman, C.A. Gaydos, M. Kundi, M. Maass, A. Makristathis, A. Meijer, R. Nadrchal, K. Persson, M.L. Rotter, C.Y.W. Tong, G. Stanek, and A.M. Hirschl, "Multicenter comparison trial of DNA extraction methods and pcr assays for detection of chlamydia pneumoniae in endarterectomy specimens," Journal of Clinical Microbiology **39**(2), 519-524 (2001).

7. M. Taniguchi, E. Akai, T. Koshida, K. Hibi, H. Kudo, K. Otsuka, H. Saito, K. Yano, H. Endo, and K. Mitsubayashi, "A fiber optic immunosensor for rapid bacteria determination," 3rd Kuala Lumpur International Conference on Biomedical Engineering 2006 **15**, 308-311 (2007).

8. M.S. John, A. Kishen, L.C. Sing, and A. Asundi, "Determination of bacterial activity by use of an evanescent-wave fiber-optic sensor," Applied Optics **41**(34), 7334-7338 (2002).

9. H.E. Giana, L. Silveira, R.A. Zangaro, and M.T.T. Pacheco, "Rapid identification of bacterial species by fluorescence spectroscopy and classification through principal components analysis," Journal of Fluorescence **13**(6), 489-493 (2003).

10. Y. Kong, S. Subbian, S.L.G. Cirillo, and J.D. Cirillo, "Application of optical imaging to study of extrapulmonary spread by tuberculosis," Tuberculosis **89**, S15-S17 (2009).

11. J.L. Kadurugamuwa and K.P. Francis, "Bioluminescent imaging of bacterial biofilm infections in vivo," Methods Mol Biol **431**, 225-239 (2008).

12. S. Wiles, K.M. Pickard, K. Peng, T.T. MacDonald, and G. Frankel, "In vivo bioluminescence imaging of the murine pathogen citrobacter rodentium," Infection and Immunology **74**(9), 5391-5396 (2006).

13. K.P. Francis, J. Yu, C. Bellinger-Kawahara, D. Joh, M.J. Hawkinson, G. Xiao, T.F. Purchio, M.G. Caparon, M. Lipsitch, and P.R. Contag, "Visualizing pneumococcal infections in the lungs of live mice using bioluminescent

streptococcus pneumoniae transformed with a novel gram-positive lux transposon," Infection and Immunity **69**(5), 3350-3358 (2001).

14. N.A. Kuklin, G.D. Pancari, T.W. Tobery, L. Cope, J. Jackson, C. Gill, K. Overbye, K.P. Francis, J. Yu, D. Montgomery, A.S. Anderson, W. McClements, and K.U. Jansen, "Real-time monitoring of bacterial infection in vivo: Development of bioluminescent staphylococcal foreign-body and deep-thigh-wound mouse infection models," Antimicrobial Agents and Chemotherapy **47**(9), 2740-2748 (2003).

15. C. Liang, M.R. Descour, K.B. Sung, and R. Richards-Kortum, "Fiber confocal reflectance microscope (fcrm) for in-vivo imaging," Optics Express **9**(13), 821-830 (2001).

16. T.J. Muldoon, M.C. Pierce, D.L. Nida, M.D. Williams, A. Gillenwater, and R. Richards-Kortum, "Subcellular-resolution molecular imaging within living tissue by fiber microendoscopy," Optics Express **15**(25), 16413-16423 (2007).

17. M. Hirano, Y. Yamashita, and A. Miyakawa, "In vivo visualization of hippocampal cells and dynamics of ca2+ concentration during anoxia: Feasibility of a fiber optic plate microscope system for in vivo experiments," Brain Research **732**(1-2), 61-68 (1996).

18. I. Smith, "Mycobacterium tuberculosis pathogenesis and molecular determinants of virulence," Clinical Microbiology Reviews **16**(3), 463-496 (2003).

19. T.R. Frieden, T.R. Sterling, S.S. Munsiff, C.J. Watt, and C. Dye, "Tuberculosis," Lancet **362**(9387), 887-899 (2003).

20. S.K. Sharma and A. Mohan, "Extrapulmonary tuberculosis," Indian Journal of Medical Research **120**(4), 316-353 (2004).

21. S. Dhandayuthapani, L.E. Via, C.A. Thomas, P.M. Horowitz, D. Deretic, and V. Deretic, "Green fluorescent protein as a marker for gene-expression and cell biology of mycobacterial interactions with macrophages," Molecular Microbiology **17**(5), 901-912 (1995).

22. E. Sagi, N. Hever, R. Rosen, A.J. Bartolome, J.R. Premkumar, R. Ulber, O. Lev, T. Scheper, and S. Belkin, "Fluorescence and bioluminescence reporter functions in genetically modified bacterial sensor strains," Sensors and Actuators B-Chemical **90**(1-3), 2-8 (2003).

23. M. Vooijs, J. Jonkers, S. Lyons, and A. Berns, "Noninvasive imaging of spontaneous retinoblastoma pathway-dependent tumors in mice," Cancer Research **62**(6), 1862-1867 (2002).

24. M. Yang, E. Baranov, P. Jiang, F.X. Sun, X.M. Li, L.N. Li, S. Hasegawa, M. Bouvet, M. Al-Tuwaijri, T. Chishima, H. Shimada, A.R. Moossa, S. Penman, and R.M. Hoffman, "Whole-body optical imaging of green fluorescent protein-expressing tumors and metastases," Proceedings of the National Academy of Sciences of the United States of America **97**(3), 1206-1211 (2000).

25. H.F. Lodish, *Molecular Cell Biology* 6th ed (W.H. Freeman, 2008).

26. G. Cox, *Optical Imaging Techniques in Cell Biology* (CRC/Taylor & Francis, 2007).

27. K.C. Maitland, H.J. Shin, H. Ra, D. Lee, O. Solgaard, and R. Richards-Kortum, "Single fiber confocal microscope with a two-axis gimbaled mems scanner for cellular imaging," Optics Express **14**(19), 8604-8612 (2006).

28. "Sumitomo electric, USA," *http://www.sumitomoelectricusa.com/scripts/products/ofig/image.cfm* (July 21, 2010).

29. M. Hirano, Y. Yamashita, and A. Miyakawa, "Development of a fiber-optic plate microscope system and visualization of cells stained with fluorescent dyes masahiko," Analytical Sciences **9**(3), 375-380 (1993).

30. A.F. Gmitro and D. Aziz, "Confocal microscopy through a fiber-optic imaging bundle," Optics Letters **18**(8), 565-567 (1993).

31. G.T. Kennedy, H.B. Manning, D.S. Elson, M.A.A. Neil, G.W. Stamp, B. Viellerobe, F. Lacombe, C. Dunsby, and P.M.W. French, "A fluorescence lifetime imaging scanning confocal endomicroscope," Journal of Biophotonics **3**(1-2), 103-107 (2010).

32. E. Laemmel, M. Genet, G. Le Goualher, A. Perchant, J.F. Le Gargasson, and E. Vicaut, "Fibered confocal fluorescence microscopy (cell-vizio (tm)) facilitates extended imaging in the field of microcirculation:- a comparison with intravital microscopy," Journal of Vascular Research **41**(5), 400-411 (2004).

33. F. Jean, G. Bourg-Heckly, and B. Viellerobe, "Fibered confocal spectroscopy and multicolor imaging system for in vivo fluorescence analysis," Optics Express **15**(7), 4008-4017 (2007).

34. A.R. Rouse and A.F. Gmitro, "Multispectral imaging with a confocal microendoscope," Optics Letters **25**(23), 1708-1710 (2000).

35. Edmund Optics. "1951 usaf glass slide resolution targets," *http://www.edmundoptics.com/onlinecatalog/displayproduct.cfm?productid=1790* (July 21, 2010).

36. "Tdtomato-our brightest red fluroescent protein," *http://www.clontech.com/images/ctq/OCT08UPD/CR8X2830_CTQOct08_tdTomato_US.pdf* (July 21, 2010).

37. N.C. Shaner, P.A. Steinbach, and R.Y. Tsien, "A guide to choosing fluorescent proteins," Nature Methods **2**(12), 905-909 (2005).

38. N.C. Deliolanis, R. Kasmieh, T. Wurdinger, B.A. Tannous, K. Shah, and V. Ntziachristos, "Performance of the red-shifted fluorescent proteins in deep-tissue molecular imaging applications," Journal of Biomedical Optics **13**(4), 044008-044016 (2008).

VITA

Nooman Sadat Mufti received his Bachelor of Technology degree in chemical engineering from the Z.H. College of Engineering and Technology, Aligarh Muslim University, India, in 2004. Following this, he entered the Molecular Engineering of Biological and Chemical Systems program at the National University of Singapore-Massachusetts Institute of Technology Alliance, Singapore and received a Master of Science degree in 2006. He then took a Process Engineer position at Wacker Chemicals, Siltronic Singapore Pte. Ltd. until 2008.

He joined the Biomedical engineering department at Texas A&M University in 2008 under the supervision of Dr. Kristen Carlson Maitland and received his M.S. in biomedical engineering in December 2010. His research interests include optical imaging and detection using techniques such as micro-endoscopy for disease prognosis and progression studies and in the areas of neural imaging for decoding the information associated with neural ensemble measurements.

Mailing address: 337 Zachary Engineering Center
3120 TAMU
College Station, TX, 77843-3120
c/o Kristen Maitland

Email: nauman.sm@gmail.com